SRON – SPEX

X-RAY SPECTROSCOPY

A Physical Background of the Software Package SPEX

SRON/SPEX/TRPB01

Version 1.0/Rev. 4.0

August 25, 1994

prepared by

R. Mewe SRON Utrecht

Summary

This paper gives a background of spectroscopy that can be performed with the software package SPEX that has been developed in the past decade at SRON-Utrecht and SRON-Leiden for the computation and modelling of X-ray and EUV spectra. It encompasses a number of subroutines for the computation of emergent spectra of optically thin plasmas such as stellar coronal loop structures and supernova remnants (also including transient ionization effects), photo-ionized plasmas, and optically thick plasmas. A synthetic spectra program that convolves the calculated input spectra with representative instrumental response functions and a subroutine for Differential Emission Measure modelling is available. The various subroutines of the spectral code are briefly considered and numerous examples of simulated spectra are given.

Contents

1 Introduction

After a general introduction to the purpose and development of the software package SPEctral X-ray and UV modelling and analysis (SPEX) we deal in some detail with radiation processes and spectral modelling in general. We give a number of examples of modelling of various optically thin or thick, transient or stationary plasmas by generating simulated spectra convolved with instrumental response functions and by applying differential emission measure modelling techniques. Finally, various subroutines of the spectral code are briefly considered.

2 Spectral code

In the last decennium SRON-Utrecht and SRON-Leiden have developed in close collaboration a software package for the calculations of X-ray spectra from hot, optically thin plasmas. This software is essentially based on the original Mewe-Gronenschild-van den Oord code (Mewe and Gronenschild 1981 (**Paper IV**), Mewe, Gronenschild, van den Oord 1985a (**Paper V**)) which includes 2167 lines from 15 different chemical elements, covering the wavelength region 1–300 Å. These lines are produced by excitation from electron impact, radiative and dielectronic recombination and by innershell excitation and ionization. In addition to the lines the code calculates the contributions from continuum radiation due to free-free, free-bound, and two-photon emission (Gronenschild and Mewe 1978 (**Paper III**), Mewe, Lemen, van den Oord 1986a (**Paper VI**)).

Our code has been applied on many occasions to optically thin plasmas, both in steady-state equilibrium (e.g. stellar coronae) and for a time-dependent ionization balance (e.g. supernova remnants) (e.g., Drake 1992). For a short description of its history and development, cf. Kaastra and Mewe (1993a).

During the last five years many improvements and extensions have been made. First, the structure of the subroutines has been sometimes drastically changed in order to allow all input/output variables to be transmitted as subroutine arguments and to significantly enhance the speed of the computations of the ionization balance (e.g. by replacing the fourth-order Runge-Kutta scheme to solve the coupled system of first-order differential rate equations by a matrix inversion; for details, e.g. Jansen 1988, Kaastra and Jansen 1993, Kaastra 1992a). Second, the accuracy of the continuum emissivity calculations was improved (Kaastra 1992a). Finally, recent extensions mainly consist of including all ions of the 30 elements from hydrogen to zinc (instead of 15 elements in the old code), updating the atomic physics, inclusion of more than 300 far ultraviolet lines between 300–2000 Å from the work of Landini and Monsignori-Fossi (1990), and the addition of about 300 dielectronic recombination and innershell excitation satellite lines of the helium- and hydrogen-like resonance lines from Fe, Ca, and Mg between 1–10 Å. The current version of the code now contains nearly 2800 spectral lines between 1–2000 Å.

Current developments are pointed to extend the work to nebular-type, photo-ionized plasmas. This will be needed since it became evident that photo-ionized plasmas play an important role in accretion-powered X-ray sources such as X-ray binaries, cataclysmic variables, and active galactic nuclei. This is where a central X-ray emitting region is surrounded by a cooler, partially ionized medium, and early-type stars where X-rays produced in shocks are transferred through a stellar wind. Moreover, atomic physics has improved considerably during the last decade, and the advent of a new series of satellites with high sensitivity and spectral resolution like *EUVE, Astro-D, SAX, AXAF*, and *XMM* strongly demands the availability of spectral codes with higher accuracy and more detail.

As a first step, the effects of innershell ionization on the spectrum and ionization balance were studied. This process (either by direct collisional ionization or photo-ionization) leads to the creation of a vacancy in one of the inner shells of the ion or atom. The vacancy is filled by a cascade of radiative (fluorescent) and non-radiative (Auger) transitions. The net result of this cascade process is the ejection of several electrons and photons, leaving the atom in a multiply ionized state. This multiple ionization has an important effect in calculations of the ionization balance in photo-ionized plasmas. We have calculated the probability distribution of ejected electrons for inner-shell ionization of all ions from Be–Zn (atomic number 4–30). Also the energy spectrum of the Auger electrons (needed for the energy balance) as well as the fluorescent photon spectrum has been calculated (Kaastra and Mewe 1993b,c).

Before we proceed with further details about the various subroutines we deal with radiation processes and spectral modelling in general (cf. e.g. Mewe 1992).

3 Radiation processes and plasma models

In nature X-rays can be produced by a variety of processes which may be classified roughly as thermal or nonthermal processes. These emission mechanisms include blackbody radiation, bremsstrahlung (thermal or nonthermal), line emission, recombination radiation, synchrotron radiation, and inverse Compton radiation (for reviews e.g. Hoover *et al.* 1972, Blumenthal and Tucker 1974).

Observations of certain features of the X-ray flux, such as its spectral energy distribution, emission lines, absorption edges, and degree of polarization, may reveal which particular emission mechanism occurs in the considered source. This information is important to the development of a feasible source model.

X-ray emission usually results from an electron-photon process. If the energy of the generating electron is thermal in nature, i.e. the electrons are described by a Maxwellian energy distribution characterized by a certain temperature T, we speak of thermal processes. Temperatures of about a million Kelvin or more are required. The most important processes are line and continuum emission from optically thin plasmas and blackbody radiation from optically thick plasmas. Nonthermal radiation is produced when the electrons are nonthermal in nature (e.g. occur in beams). The most important processes for nonthermal X-ray radiation in cosmic sources involve the acceleration of (relativistic) electrons in magnetic fields (synchrotron radiation or magnetic bremsstrahlung) and the interaction of high-energetic electrons with visible, infrared, or microwave photons (inverse Compton radiation). Nonthermal electrons may also produce bremsstrahlung and line emission by deceleration as a result of Coulomb interaction with ions when electron beams traverse the plasma in a Solar or stellar flare (e.g. Brown 1971, Švestka 1976). In Table 1 the processes and some examples of sources in which they may occur are summarized.

It is instructive to consider several basic plasma models. Astrophysical plasmas are usually discussed in terms of three (thermal) models: (i) Coronal model, (ii) Nebular model, (iii) Atmospheric model, or in terms of combinations thereof (cf. Table 2). As a fourth model we might consider relativistic plasmas in which electron-positron pair production in photon-photon interactions dominate.

The optically thin model was first applied by Elwert (1952) to the Solar corona and is therefore also designated *"the coronal model"*. *The nebular model* owes its name to the fact that it is the X-ray analogue of a planetary nebula, in which a central continuum source ionizes the surrounding gas (e.g. McCray 1984). This and the optically thick atmosphere model can be applied to the

Table 1: **Production mechanisms of X-rays in cosmic sources**

A. Thermal processes
Radiation produced by electron-ion interactions, characterized by some gas temperature T (essentially the **electron** temperature) which should be $\gtrsim 10^6$–10^7 K for X-ray production.

• A.1. **Blackbody** radiation from hot, **optically thick** plasma of surface temperature T. Continuous **energy** spectrum: $E^3/[\exp(E/kT)-1]$ (sometimes as **modified quasi-BB** radiation reprocessed by scattering in the gas). E.g. *compact X-ray binaries, cataclysmic variables, isolated white dwarfs, active galactic nuclei (AGNs).*

• A.2. Radiation from hot, **optically thin coronal** plasma. E.g. *stellar coronae, supernova remnants (SNRs), hot interstellar matter, intracluster gas, normal galaxies and galactic halos.*

• A.2.1. **Thermal bremsstrahlung** continuum produced by a transition of a free plasma electron between two continuum states of the ion: energy spectrum $\propto T^{-\frac{1}{2}}\exp(-E/kT)$. Dominant at $T \gtrsim 10^8$ K.

• A.2.2. **Discrete line** emission (electronic transition between two bound levels of the ion). Dominant at $T \lesssim 5\ 10^7$ K. Collisionally excited spectral lines from highly ionized atoms are signatures of the thermal nature of the plasma.

• A.2.3. **Radiative recombination** continuum (capture of the electron into a bound state of the ion) with emission edges that fade out for $T \gg 10^7$ K, where bremsstrahlung dominates.

• A.2.4. **Dielectronic recombination** lines (capture of a free electron into a doubly excited ion state through simultaneous excitation of a bound electron of the ion).

• A.2.5. **Two-photon** continuum (simultaneous emission of two photons from a metastable state).

N.B. The first two processes are usually the most important ones.

• A.3. Radiation from **nebular-type photoionized** plasma. E.g. compact X-ray source embedded in colder gas. Continuum spectrum with superimposed recombination lines and narrow recombination continua. When the plasma becomes opaque for Compton scattering, Comptonization, reflection and fluorescence occur (e.g. in and around accretion disks around black holes).

B. Nonthermal processes
Interaction of relativistic electrons with magnetic fields (**synchrotron or cyclotron** radiation), interaction with visible, infrared and microwave photons that are upgraded to X-ray photons (**inverse Compton** scattering), or interaction of nonthermal electrons with ions (**nonthermal bremsstrahlung**). E.g. *nebulae, intergalactic space, radio galaxies, AGNs, diffuse background, compact objects and Solar and stellar flares.*

• B.1. **Synchrotron** radiation with continuous, polarized energy spectrum $E^{-\alpha}$ (energy spectral index $\alpha = (s-1)/2$ where s is index of the power-law electron number distribution per unit energy range; e.g. $\alpha \simeq 1$ for Crab Nebula). For **nonthermal** bremsstrahlung in Solar/stellar flares $\alpha = (2s-1)/2$. In a strong magnetic field at the surface of neutron stars ($B \sim 10^{12}$ G) **cyclotron resonance** absorption occurs in the X-ray region. E.g. *X-ray pulsars, γ-ray bursts.*

• B.2. **Inverse Compton** radiation. Continuous power law spectrum, spectral energy index $\alpha = (s-1)/2$. In some cases low-energy photons produced by the synchrotron process may be transformed into X-rays by inverse Compton scattering (**Compton-synchrotron** radiation), e.g. in *compact radio sources* and *AGNs.*

• B.3. **Positron annihilation** emission line at 0.511 MeV in hot magnetized plasma near the surface of a neutron star. The energy is reduced by $\sim 10\%$ due to gravitational redshift.

Table 2: **Comparison between various models**

	Coronal Model	**Nebular Model**	**Atmospheric Model**
Assumptions	Optically thin; collisional ionization & collisional excitation dominate	Optically thin/thick (sometimes electron scattering important) photo-ionization and photo-excitation by radiation from an external X-ray source	Optically thick collisional ionization
Examples	- stellar coronae - SNRs - clusters of galaxies - central region of AGN?	- compact objects (WD, NS, BH in X-ray binaries) - stellar winds - AGNs	- photosphere of hot O stars - hot DA dwarfs - NS
Model parameters	- EM=$\int n_e^2 dV$ or - $DEM = n_e^2 dV/dT$ - T (controlled externally) - n_e (density-sensitive lines)	- ξ=L_X/nr^2 (ionization par.) - $(L_X n)^{1/2}$ (contin. opt. depth) - n_e (T is not a free parameter)	- $T_{\rm eff}$ - g - abundances
Characteristics	Spectra rich of emission lines excited by electron collisions; He-like singlet/triplet ratio & Fe XVII-XIX lines can be used to discriminate between coronal/nebular model	Spectra with emission and absorption lines formed by recombination; *many* ion stages at low T	Spectra with ionization absorption edges/lines and continuum
Problems	- atomic rates - non-stationary ionization balance	T is not a free parameter, but is determined by local energy equations	- NS comptonization (Monte Carlo calc.) - layered atmosphere - non-LTE effects
Results	- $T, (D)EM, n_e$,abundances	- $n_{(e)}$,abundances	- $T_{\rm eff}$, g,abundances

important classes of X-ray binary sources containing a compact object, such as a white dwarf (WD), neutron star (NS), or black hole (BH). In practice we may encounter a mixture of all models because in many cases the observed sources are not spatially resolved which impedes the disentanglement of emission regions with different model properties. For example, spectral observations with the medium-resolution Objective Grating Spectrometer (OGS) on the *EINSTEIN* observatory of 22 bright galactic X-ray binaries (Vrtilek *et al.* 1991) revealed in many cases the presence of several line emission and absorption features. The observed line emission suggests that the emitting material spans a large range in temperatures and ionization states. Neither photoionization nor coronal models can reproduce the relative line intensities. This can be caused by simultaneous observation of features associated with both models, i.e. the line emission may originate from two distinct regions that cannot be spatially resolved in the observations: a) a collisionally excited, coronal region and b) a photo-ionized region that is excited directly by the central X-ray source. Moreover, there may be a contribution to the spectral (power-law) continuum of the central hard X-ray source by soft X-rays from possibly reprocessed blackbody radiation from the optically thick accretion disk. The measurement of line velocities as a function of binary phase with future high-resolution spectrometers onboard *AXAF* and *XMM* would greatly facilitate the disentanglement of the different line emission regions.

4 Spectral modelling

Certain models are needed to infer from the observations the relevant physical parameters including electron temperature, emission measure and density distributions, ion and elemental abundances, mass motions, and the nature of the ambient radiation field.

The usual procedure is to apply a forward modelling technique by convolving theoretical model spectra with the instrumental response and to vary the model parameters in order to optimize the fit of the model to the observational data. A common approach is to consider first a simplified plasma model for the X-ray source, neglecting much of the complexity of the temperature and density structure and of the effects of opacity, and to synthesize such models into successively more sophisticated approximations of the source model.

In Figure 1 we give in a processing flow diagram schematically the process of spectral modelling for the case of optically thin coronal plasmas. The synthetic spectra program is fed with input parameters from the spectral model (atomic data for ionization and line and continuum excitation), the instrumental model, and from the assumed plasma model for the source. The synthetic spectra code generates spectra which can be compared to the observations and tested by means of statistical fitting procedures.

Let us consider an optically thin plasma source model. To represent an optically thin source such as a stellar corona or a supernova remnant (SNR) we may start with a simple single-temperature model or as a next step a two-temperature model, or a more sophisticated multi-temperature, differential emission measure (DEM) model (e.g. Lemen *et al.* 1989). Once we have obtained more insight into the temperature stratification of the source we may let supersede such models by a more specific physical model which also may contain the plasma dynamics. For a plasma in a transient state (e.g. SNR, impulsive phase of a flare) we have to introduce a *time-dependent* model. In the following paragraphs we deal first in detail with the optically thin model and then give several examples representative for this optically thin model and other models like photo-ionized plasma and optically thick plasma.

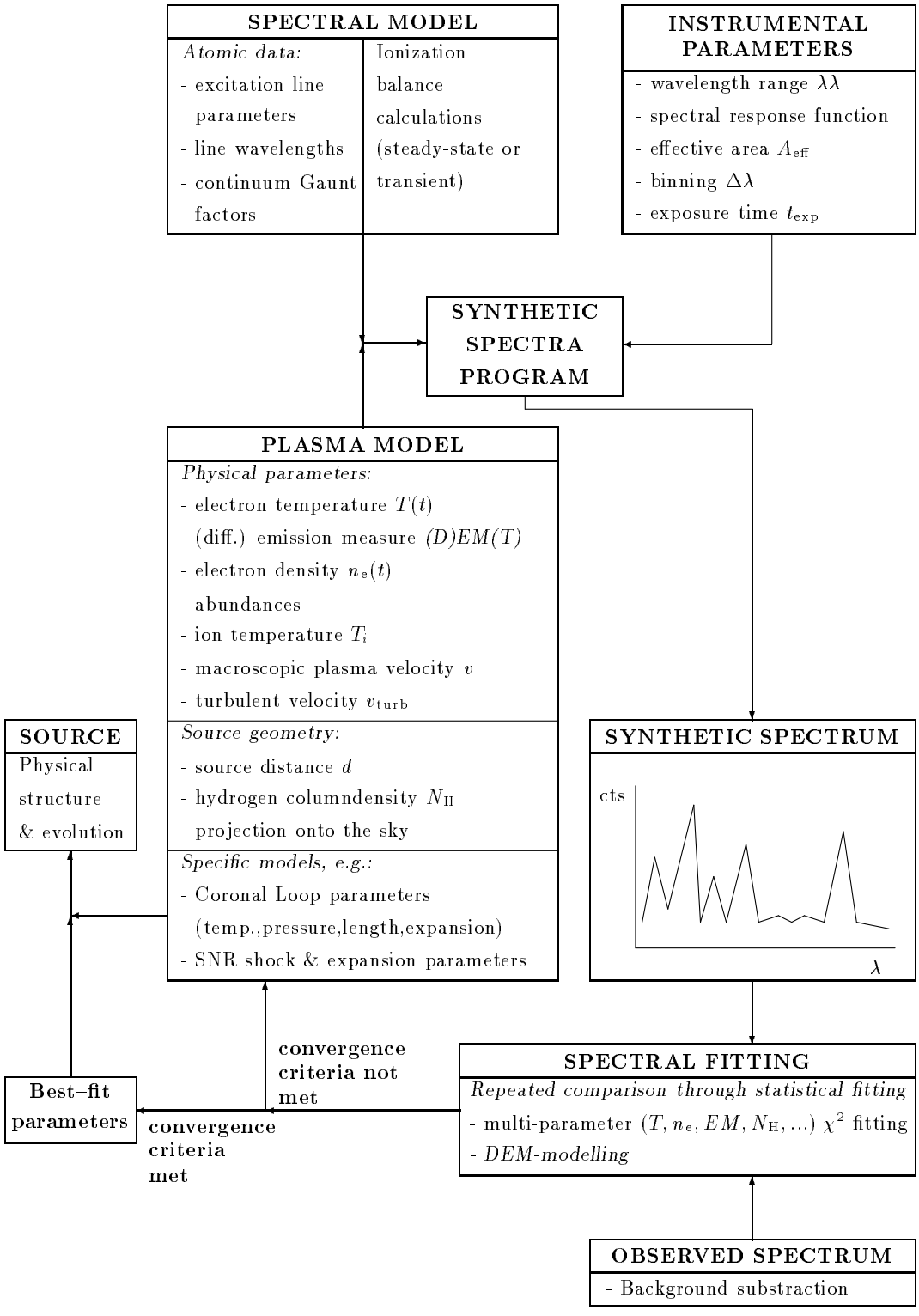

Figure 1: Processing Flow Diagram for Spectral Modelling of optically thin plasmas (from Mewe 1992).

5 Optically thin thermal plasma

The X-ray emission from a stellar corona is typically optically thin thermal plasma emission from a very hot, tenuous, and highly ionized gas in which the atoms have all, or almost all, of their electrons stripped due to collisions with energetic electrons. Temperatures are typically above one million degrees Kelvin.

This is the standard *coronal model* that was first applied by Elwert (1952) to the Solar corona. It assumes that the radiative power loss is compensated by heating so that the gas is in a steady state of statistical equilibrium both for the bound atomic states and for the ionization balance. The electron collisions control the ionization state and emissivity of the gas and the plasma electrons (and ions) are relaxed to Maxwellian energy distributions with a common temperature, T, a free parameter controlled by external processes (e.g. Mewe 1990a). The relaxation time for electron-electron collisions ($t_{ee} \approx 0.01 T^{3/2} n_e^{-1}$ (s); T in K, electron density, n_e, in cm^{-3} (Spitzer 1962)) is generally short enough to ensure a Maxwellian velocity distribution for the electrons, unless the timescales for energy loss or gain or particle containment are smaller than t_{ee}.

The heat input is directly coupled to the electrons and ions. If the heating mechanism preferentially heats one kind of particles (e.g., heavy ions in shocks or electrons in microturbulent plasmas) and if the Coulomb collision equilibration time ($t_{ei} \approx 10\ T^{3/2} n_e^{-1}$ (s) (Spitzer 1962)) is long enough, the ion and electron temperatures may differ significantly ($T_i \neq T_e$). However, if in this case plasma instabilities reduce the equilibration timescale then $T_i \simeq T_e$ (e.g. in turbulent shocks in supernova remnants) (Mewe 1984).

Deviations from the coronal model due to effects of photo-ionization, optical depth, high density, non-Maxwellian electron distributions, and transient ionization are discussed by Raymond (1988) and Mewe (1990a,b).

Examples of "coronal" plasmas are: stellar coronae, supernova remnants, the hot gas in the interstellar medium and in galaxies and clusters, and possibly also tenuous intercloud gas pervading the central region in active galactic nuclei (for examples of various X-ray spectra, e.g. Mewe 1990b).

5.1 Ionization balance

Much of the temperature sensitivity of the soft X-ray spectrum is associated with the ionization structure. Under the assumptions of the coronal model, nearly all ions can be taken to be in their ground states. The ionization state is then controlled by electron impact ionization (including sometimes a contribution from autoionization) and by radiative plus dielectronic recombination. The rate of change of the population density $N_{Z,z}$ (in cm^{-3}) of ion Z^{+z} from element of atomic number Z is given by

$$\frac{dN_{Z,z}}{n_e dt} = N_{Z,z-1} S_{Z,z-1} - N_{Z,z}(S_{Z,z} + \alpha_{Z,z}) + N_{Z,z+1}\alpha_{Z,z+1}, \qquad (1)$$

where $S_{Z,z}$ and $\alpha_{Z,z}$ are the total ionization ($z \rightarrow z+1$) and recombination ($z \rightarrow z-1$) rate coefficients (in cm^3 s^{-1}) of ion Z^{+z}, etc. In the general case of a time-dependent plasma the ionization structure can be derived by solving for each element Z a set of $Z+1$ coupled rate equations. The population of stage z depends on the four rates which connect it with the neighbouring ionization stages $z-1$ and $z+1$. For the special case of a steady-state equilibrium the rate of change (left-hand member of

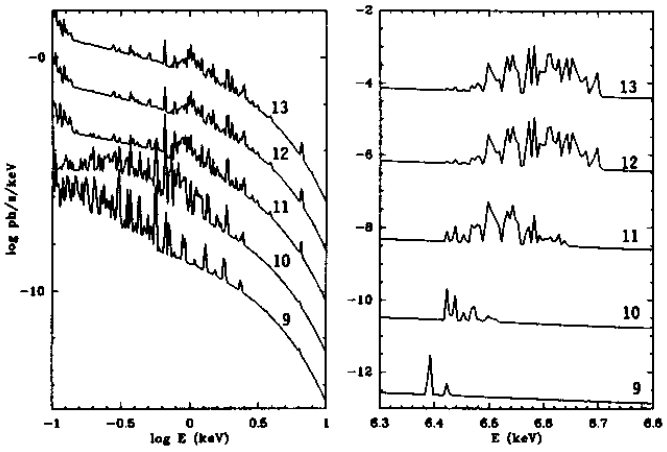

Figure 2: X-ray spectra between 0.1–10 keV (left panel) and around the Fe K complex (right panel) of an optically thin transient plasma that has been heated instantaneously to 10 MK at time $t = 0$, for values of the ionization parameter $\log(n_e t)(\mathrm{cm}^{-3}\ \mathrm{s})$ of 9, 10, 11, 12, and 13 (bottom to top) (from Kaastra and Bleeker 1991). This is an example of a calculation with the NEI subroutine.

Eq. (1)) can be set equal to zero, and the population density ratio $N_{Z,z+1}/N_{Z,z}$ of two adjacent ion stages $Z^{+(z+1)}$ and Z^{+z} can be expressed by

$$\frac{N_{Z,z+1}}{N_{Z,z}} = \frac{S_{Z,z}(T)}{\alpha_{Z,z+1}(T)}, \tag{2}$$

which is, to first order, only dependent on T and not on n_e, as long as stepwise ionization in $S_{Z,z}$ and collisional coupling to the continuum levels in $\alpha_{Z,z+1}$ can be neglected (e.g. Mewe 1970, Wilson 1962).

For a discussion of the ionization and recombination processes, see e.g. Mewe (1988, 1990a) and Raymond (1988, 1990).

5.1.1 Ionization balance in a transient plasma

The assumptions of steady-state coronal equilibrium are not always valid for cosmic X-ray sources. The plasma approaches the equilibrium expressed in Eq. (2) over a relaxation time, t_{rel}, comparable to the ionization and recombination times of the relevant ion. When the physical plasma parameters change quickly due to a variety of processes such as plasma instabilities, shock compression, rapid expansion, heating or cooling of the gas, etc., the assumptions of a steady-state equilibrium break down and the plasma is considered to be in a *transient* state. For example, in cases where the electron density is very low, the time scale t_{rel} for ionization equilibrium to be established at the currently existing electron temperature may greatly exceed the relevant dynamical plasma time scale, t_{pl}, on

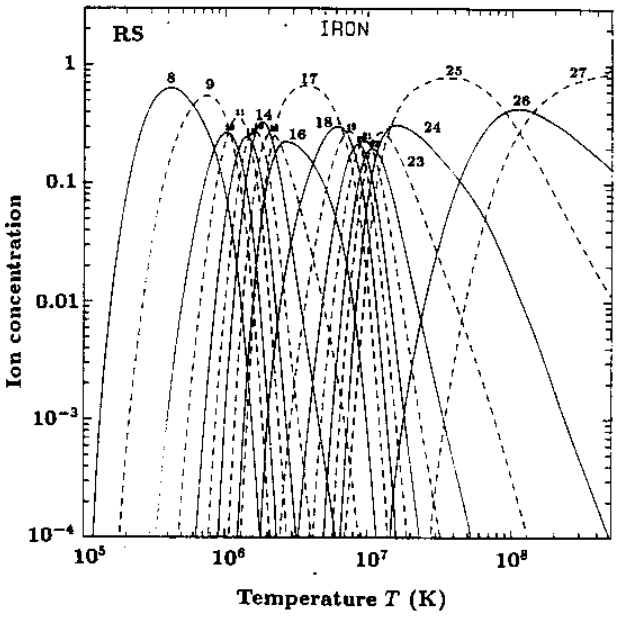

Figure 3: Iron ionization structure appropriate to a collisionally dominated optically thin coronal plasma as a function of electron temperature. RS = Raymond-Smith (1977) calculations. Ion stages are designated by numbers: 8 = Fe VIII, etc. (from Mewe 1991a).

which *heating* or *cooling* takes place, hence on which the relevant plasma parameters (T, n_e) may vary (e.g. calculations for shocks in supernova remnants (SNRs): Shapiro and Moore 1976, Hamilton et al. 1983, Gronenschild and Mewe 1982, Itoh 1984, Mewe 1984); Solar flares: Shapiro and Moore 1977, Mewe and Schrijver 1980, Mewe and Gronenschild 1981, Mewe *et al.* 1985b). Then the establishment of the ionization balance lags behind the temperature changes and as a result the plasma is *under-* or *over*-ionized compared to the equilibrium state belonging to the instantaneous temperature. This may have dramatic effects on the emergent X-ray spectrum (e.g. soft X-ray *excess* or *deficit* and *enhanced* or *decreased* radiative cooling). From Eq. (1) we can notice that the main parameter to generally characterize this non-equilibrium is the time integral of the electron density, often denoted by $n_e t$, the *ionization parameter*. Figure 2 shows a series of spectra of an optically thin transient plasma that has been heated instantaneously to 10 MK at time $t = 0$, for values of $\log(n_e t)(\mathrm{cm}^{-3}\,\mathrm{s})$ (bottom to top) of 9, 10, 11, 12, and 13 (Kaastra and Bleeker 1991). The figure shows that most of the line emission and also the effective line centroid of the Fe K-complex shifts towards higher energy when $n_e t$ increases: as ionization progresses, elements with higher Z become ionized.

As a result, such a nonequilibrium gas as for example a rapidly heated SNR or flare plasma will initially radiate thermal bremsstrahlung characteristic of the high temperature (in a cosmically abundant plasma the X-ray spectrum is mainly produced by collisions of the hot electrons with protons and *alpha*-particles, hence virtually independent of the ionization balance) together with line plus two-photon and free-bound emission characteristic of the nonequilibrium ionization (NEI) structure corre-

sponding to the preheating state. The line spectrum is therefore much softer than the bremsstrahlung continuum and as the gas ionizes out, this NEI enhancement of the soft X-rays will eventually disappear, with spectral hardening occurring along the way. To study such effects in Solar or stellar flares, high-resolution spectroscopy must be applied (e.g. Mewe et al. 1985b). Resonance/innershell excitation satellite line ratios (cf. Mewe 1988) and line/continuum ratios (e.g. Shapiro and Moore 1977) can be used as indicators of deviations from ionization equilibrium. For further discussions, e.g. Mewe (1984, 1990a).

5.2 Spectra

The line emission - that dominates the soft X-ray spectrum and the cooling of coronae at temperatures up to $\sim$ 10 MK - comes mainly from the excitation by the impact of a free electron of an electronic transition between bound levels within a highly ionized atom, followed by the spontaneous radiative decay from the upper line level (cf. Mewe *et al.* 1985a). Continuum emission in optically thin plasmas is produced by the interaction of a free electron with an ion either by a free-free (ff) transition between two continuum states of the ion ("bremsstrahlung"), a free-bound (fb) transition (capture of the electron into a bound state of the ion), or a two-photon process (2γ) (excitation of a metastable level in a hydrogen- or helium-like ion followed by the simultaneous emission of two photons) (cf. Mewe et al. 1986a).

The overall appearance of the X-ray spectra will be dominated by the ionization structure which varies dramatically with temperature throughout the range 0.1–100 MK as is shown for example in Figure 3 for the ionization structure of iron and in Figure 4 which compares calculated incident photon flux spectra between 3–140 Å at $T = 4$ MK with spectra convolved with the response of the high-resolution Low Energy Transmission Grating Spectrometer (LETGS) on *AXAF* (Brinkman et al. 1987) and the medium-resolution Transmission Grating Spectrometer (TGS) on *EXOSAT* (Brinkman et al. 1980).

Figure 5 illustrates the possibilities of high-resolution X-ray spectroscopy for the studies of stellar coronae. For a number of prototype stars we have calculated spectra between 3–140 Å convolved with the response of the high-resolution Low Energy Transmission Grating Spectrometer (LETGS) on *AXAF* (Brinkman *et al.* 1987) and for an exposure time of 10^4 s. The source parameters used for these simulations are derived from *EXOSAT*, *EINSTEIN*, and *ROSAT* observations (listed in Table 1 of Mewe (1992b) and Table 3 of Mewe (1991a)). The spectra have been calculated with our optically thin plasma code and convolved with the instrumental response with the synthetic spectra program.[1] For calculating the interstellar absorption we have used data from Morrison and McCammon (1983) (with a correction of their polynomial fit between 4–7 keV). At low energies (< 0.03 keV, $\gtrsim 400$ Å) we use data from Cruddace *et al.* (1974). It is clearly seen that the improved spectral resolution ($\Delta\lambda \simeq 0.05$ Å) of the *AXAF* spectrometer allows to resolve virtually all important spectral lines yielding the possibility to resolve the coronal temperature and ionization structure in more detail and to determine abundances from line/line and line/continuum ratios.

In extremely hot ($T > 100$ MK) plasmas all abundant elements are nearly fully ionized and the X-ray emission is dominated by the free-free continuum from hydrogen and helium, although Fe K-shell emission around 1.8 Å still persists as a prominent feature up to temperatures of a few 100 MK. With decreasing temperature the heavier trace elements are only partly ionized, beginning with iron, and

[1] We note that for the calculations we use the instrumental data appropriate to the original baseline design with six telescope mirrors, though recently the mission design has been reconfigured into two separate missions: a) *AXAF-I* (=imager) with 4 telescope mirrors containing the grating spectrometers, and the HRC and CCD cameras, b) *AXAF-S* (=spectrometer) containing the bolometer and a foil spectrometer.

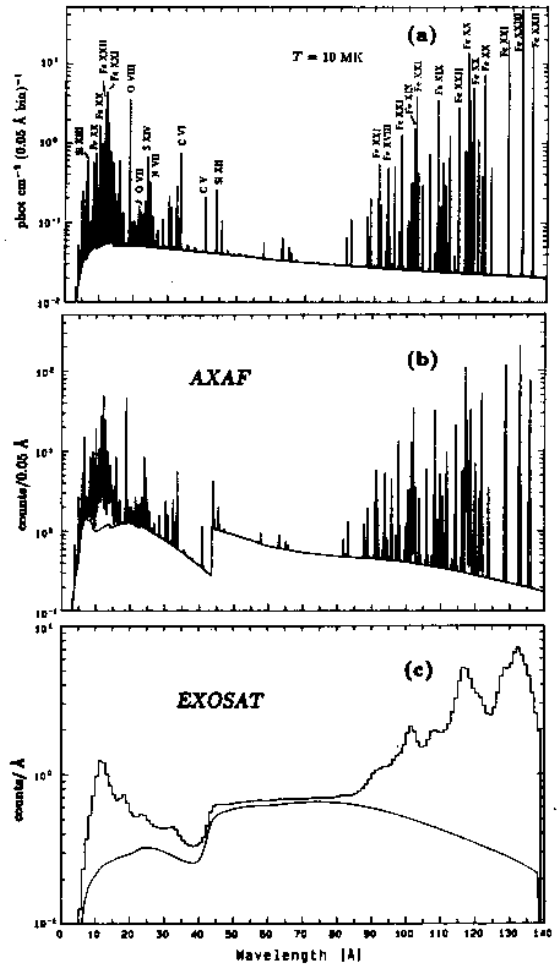

Figure 4: Incident photon flux spectrum, integrated over 10^4 s, calculated for an optically thin plasma with temperature $T = 4$ MK and reduced emission measure $EM/d^2 = 10^{50}$ cm^{-3} pc^{-2}. The most prominent lines are labelled with the corresponding ion species. Panels b and c: Spectra convolved with the response of $AXAF$-LETGS and $EXOSAT$-TGS, respectively. Upper curve in panel c gives total line plus continuum spectrum, whereas bottom curve represents the contribution from continuum radiation only (from Mewe 1990b). This is an example of the convolution of a theoretical input spectrum with specifically chosen instrumental response functions in the synthetic spectra program.

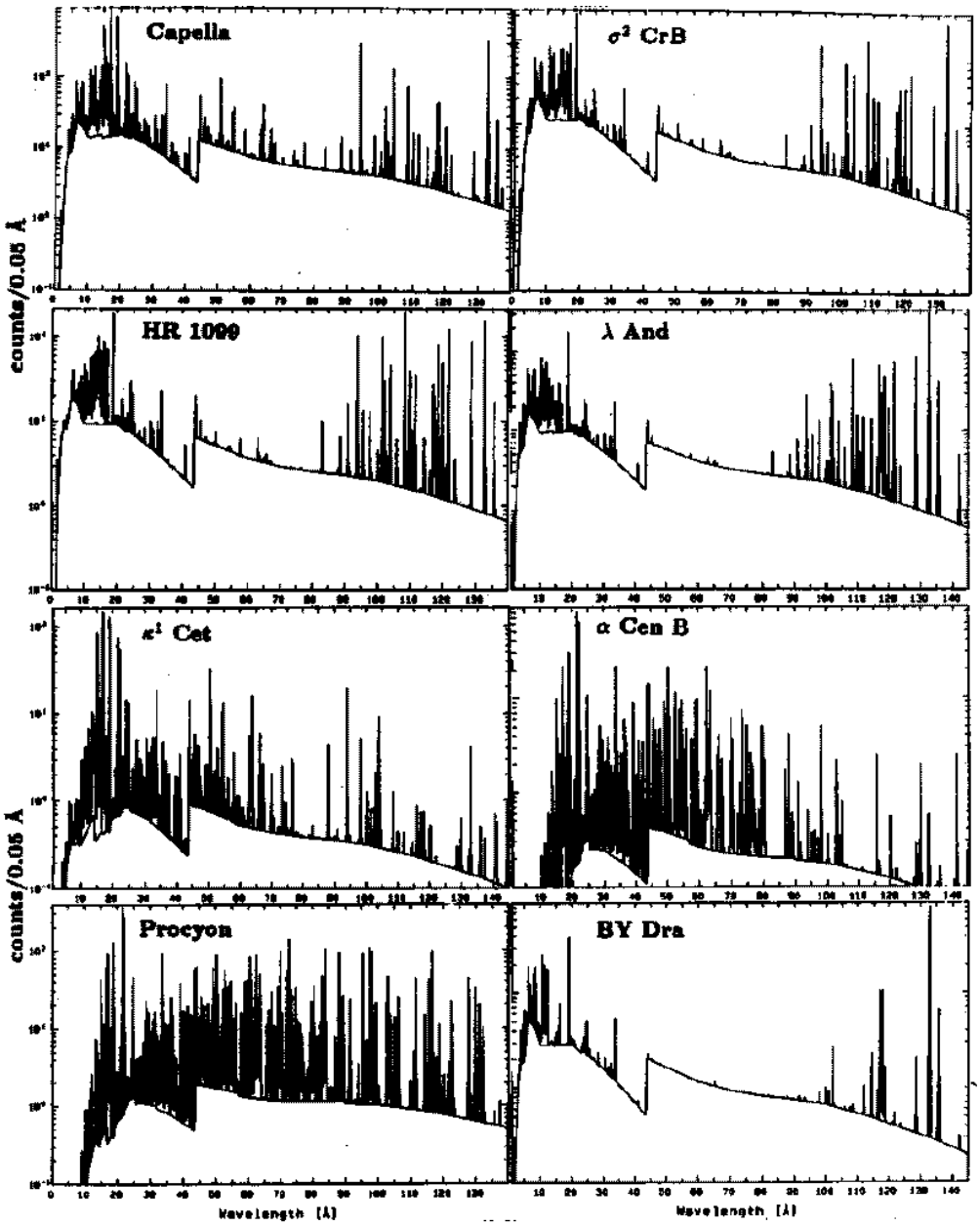

Figure 5: X-ray spectra of various stellar coronal sources simulated for the $AXAF$ Low Energy Transmission Grating Spectrometer (LETGS). Exposure time is 10^4 s. Note the logarithmic scale for the observed counting rates (from Mewe 1992b).

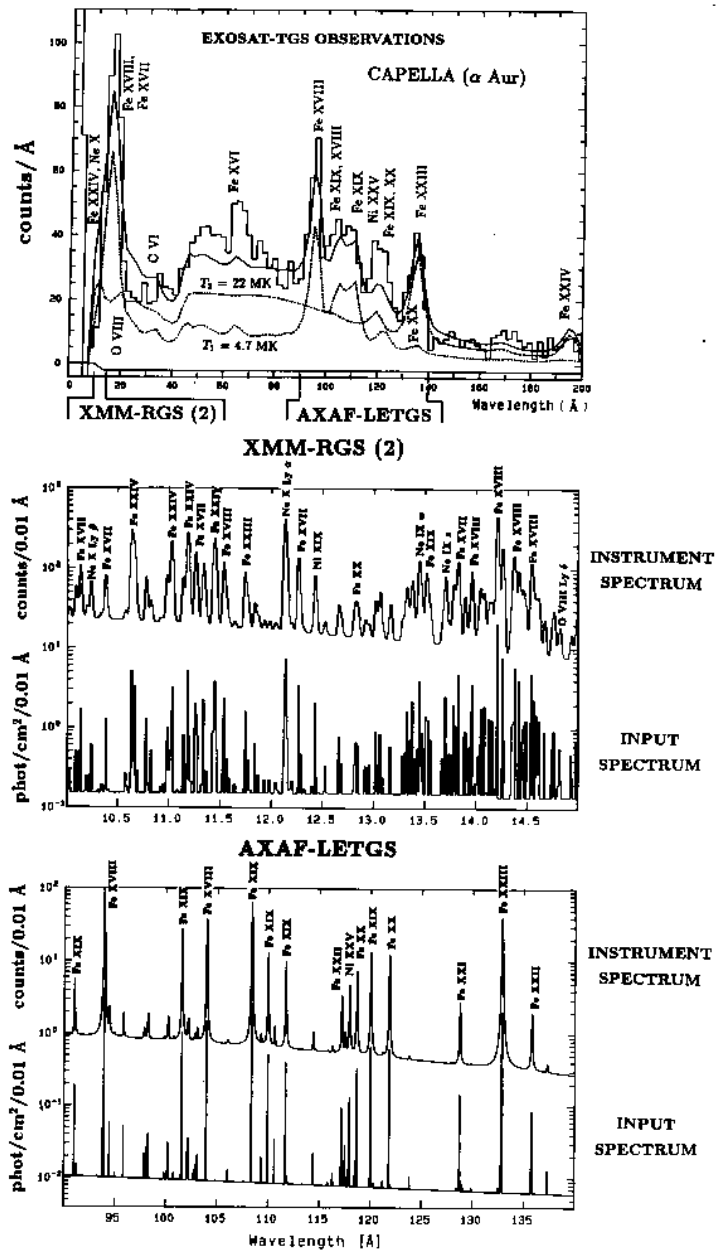

Figure 6: Comparison between *EXOSAT*-TGS observations of Capella (t_{exp} = 8.5 10^4 s, backgr. of 21.8 c/Å subtracted) and simulations in a blow up in the wavelength regions 10–15 Å (*XMM*-RGS (second order)) and 90–140 Å (*AXAF*-LETGS). Exposure time t_{exp} = 10^4 s. Note the increase in sensitivity relative to *EXOSAT* of *AXAF* and *XMM* by one or two orders of magnitude, respectively (from Mewe 1991a).

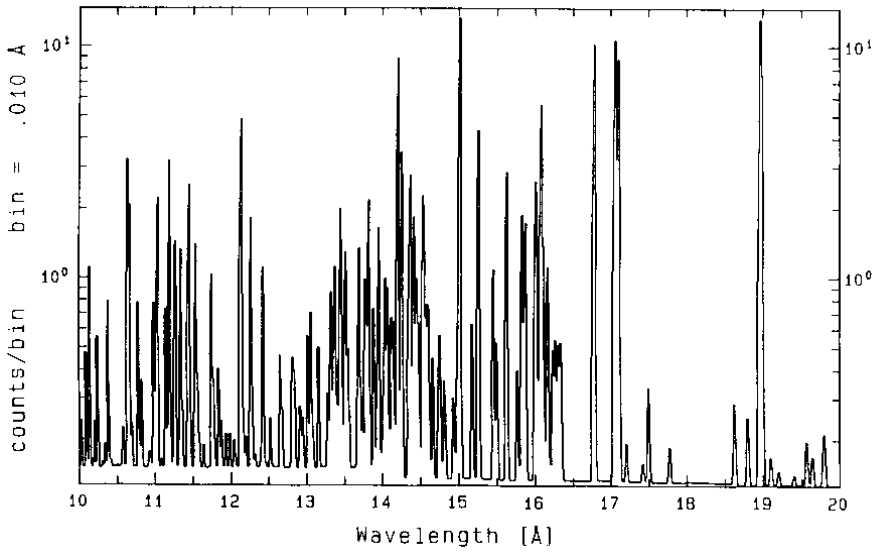

Figure 7: Simulated spectrum of Capella as measured in 10^4 s with an SIS-junction detector with a resolving power $R \sim 700$ (SIS = superconductor-isolator-superconductor).

spectral emission lines excited by electron collisions show up and will begin to dominate the X-ray spectrum. This is especially true for the Fe L-shell lines around 15 Å, the Fe K-shell lines at ~ 2 Å and the Fe $2s$–$2p$ lines around 100 Å. In a wide temperature range (0.01–10 MK) the X-ray spectra of optically thin sources are rich in emission lines from many ions, so that high-resolution X-ray spectroscopy has its most obvious application in diagnosing optically thin sources such as the coronae of late-type stars.

5.2.1 Simulations of high-resolution Fe K and L spectra

The high spectral resolution ($\lambda/\Delta\lambda \gtrsim 1000$) of the next generation of dispersive and non-dispersive spectrometers on board *AXAF* and *XMM* is needed to fully resolve the temperature structure of optically thin plasmas like stellar coronae and supernova remnants. In the following we give some examples of high-resolution iron L-shell and K-shell spectra.

Figure 6 compares between spectra of Capella measured with the transmission grating spectrometer (TGS) on *EXOSAT* (Lemen *et al.* 1989, Mewe 1991a) and spectra simulated for the LETGS on *AXAF* (Brinkman *et al.* 1987) and the reflection grating spectrometer (RGS) on *XMM* (Brinkman *et al.* 1989). The simulated spectra of the Fe L-shell blend around 15 Å (2ℓ–$\geq 3\ell'$ lines) and of the strong $2s$–$2p$ lines between 90–140 Å clearly demonstrate the diagnostic capabilities of the instruments and show that spectrometers with a resolving power of $\gtrsim 500$ up to $\sim$1000 or more resolve the L-blend in its

many individual components, allowing more refined temperature, density, and velocity diagnostics.

In Figure 7 we present a simulation of the spectrum of Capella as measured with a SIS-junction detector with a resolving power $R \sim 700$. It is clearly seen that such a measurement will allow the resolution of a lot of individual lines associated with different ionization stages (hence temperatures). With such detectors placed in an array also imaging is possible which provides a powerful diagnostic tool for the observation of the detailed temperature and density structure of extended sources such as supernova remnants.

The high-resolution X-ray K-shell spectra from highly ionized iron and calcium in the wavelength regions 1.7–2 Å and 3–3.3 Å provide superior diagnostics of very hot plasmas with temperatures in the range 10–100 MK. The availability of such spectra of the flaring Sun as obtained with the Bragg crystal spectrometers aboard the spacecrafts *P78-1*, *SMM*, and *Hinotori* (for detailed references cf. Mewe (1991a)) has stimulated the diagnostics of hot thin plasmas. Up to now the iron K-shell blend at 6.7 keV has been detected from *non-solar* stellar coronae only at rare occasions: e.g. in *EXOSAT* ME observations on Algol (White *et al.* 1986, van den Oord and Mewe 1989) and UX Ari (Pasquini *et al.* 1988) and *GINGA* LAC observations on UX Ari (Tsuru *et al.* 1989).

In high-resolution spectra the temperature can be diagnosed from the helium-like singlet/triplet ratio or for very hot plasmas from the intensity ratio of the Fe XXVI Ly α and Fe XXV w He-like resonance line. The technique of measuring the ratio of the resonance line and a nearby dielectronic recombination satellite line has been widely used in these short-wavelength regions to derive the solar flare temperature from very high-resolution X-ray spectra. The helium-like triplets with their satellites provide a very valuable diagnostics for electron temperature, emission measure, abundances, and ionization balance. However, an extremely high spectral resolution is required in order to avoid too much blending of the stronger line features that are most important for the diagnostics of the plasma parameters by the hundreds of weaker unresolved satellite lines. In case of rather serious blending a more precise determination of the electron temperature will require a profile fitting of the entire spectrum (e.g. Antonucci *et al.* 1982, Tanaka 1986). In addition to the temperature, the (differential) emission measure (distribution) EM ($\varphi(T)$) can be derived from the line intensities or from the complete spectral fitting.

In order to demonstrate the effects of spectral resolution we have simulated the spectrum of the K-shell spectrum of helium-like iron and its satellites in the interval 1.84–1.92 Å for a series of resolving powers $R = \lambda/\Delta\lambda$ (cf. also Schmitt (1990)). The calculations incorporate about 150 lines in this wavelength region. A gaussian instrumental profile with a FWHM of $1.85/R$ Å is assumed and the lines are assumed to be broadened by thermal Doppler broadening (which corresponds to a resolution $R_D = \lambda/\Delta_D \simeq 1000\ (T/100\ \mathrm{MK})^{-1/2}$). The electron temperature is chosen to be $T = 10$ MK (corresponding to $R_D = 3300$). Figure 8 shows the results for the photon flux in 0.0002 Å bins integrated over 10^4 s for a temperature $T = 10$ MK and reduced emission measure $\varepsilon/d^2 = 10^{50}$ cm^{-3} pc^{-2}.

We start with a very high instrumental resolving power of $R = 10^4$ (Figure 8, panel a) (typical for the Bragg crystal spectrometers flown on *P78-1* (SOLFLEX), *SMM* (BCS) and *Hinotori* (SOX2). In this case the resolution is mainly determined by the Doppler line broadening. Line identifications are given following Gabriel's (1972) notation for the helium-like Fe XXV lines (w = resonance, x, y = intercombination, z = forbidden line) and lithium-like Fe XXIV lines. The dielectronic recombination (DR) Fe XXIV satellite/Fe XXV resonance line ratio j/w is particularly important, because it depends strongly on the electron temperature and is independent of the ionization balance. On the other hand, the innershell excitation (IE) Fe XXIV satellite/resonance line ratio q/w determines the ratio of the densities of the Fe XXIV and Fe XXV ions and can be used to measure departures from coronal ionization equilibrium. In the spectrum we also indicate the strongest pairs of IE and DR satellites

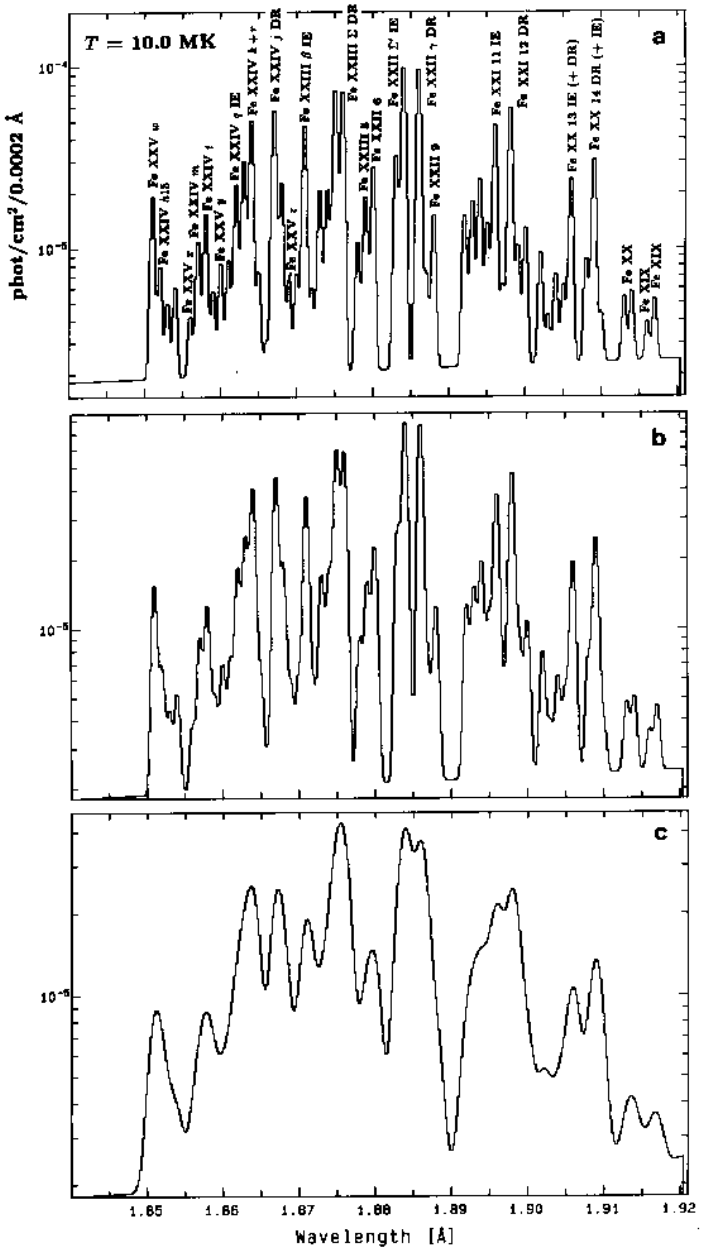

Figure 8: Simulated Fe K-shell spectra for an optically thin coronal plasma at a temperature $T = 10$ MK ($EM/d^2 = 10^{50}$ cm^{-3} pc^{-2}, $t_{exp} = 10^4$ s) for several resolving powers R ($\equiv \lambda/\Delta\lambda$): 10000 (panel a); 3300 (b); 1000 (c), corresponding approximately to those obtained in: *P78*-SOLFLEX, *SMM*-BCS, *Hinotori*-SOX2 (a); SOX1 and the theoretical limit for calorimeter and Nb-junction (b); expected performance of *AXAF* calorimeter (c). For notations of line identifications see text.

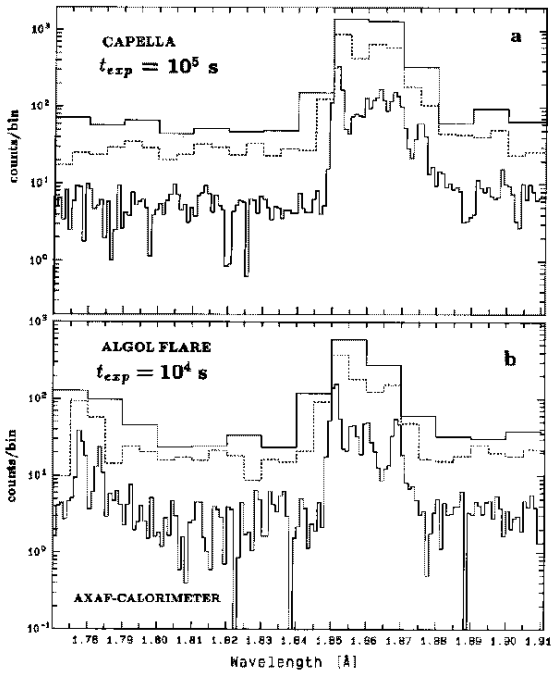

Figure 9: Simulated *AXAF* bolometer (or calorimeter) spectra with random noise added of Capella (panel a) and of a flare on Algol (b) for an exposure time of $t_{exp} = 10^5$ s and of 10^4 s, respectively, and with wavelength bins of 0.001 Å, 0.005 Å, and 0.01 Å.

from Fe XXIII–Fe XIX, which can also be used to determine T, EM, and (departures from) ionization equilibrium (notations are from Doschek *et al.* 1981). The typical splitting of the lines is $\sim$ 0.001 Å, so that we need a typical resolving power of $\gtrsim$ 2000 to have full profit of the diagnostics.

In the next step we degrade the resolution until $R = 3300$ (i.e. $\Delta E \simeq 2$ eV, typical for SOX1 on *Hinotori* and nearly corresponding to the theoretical limits to be attained for the microcalorimeter (e.g. Linsky 1990) and Nb-junction solid-state detector) (see Figure 8, panel b). We see that for most lines little information is lost, though the q line becomes somewhat blended by nearby Fe XXIII satellites and the dielectronic recombination Fe XXIV k line. Finally, at $R = 1000$ (Figure 8, panel c) (ΔE = 7 eV, e.g. expected for the calorimeter proposed for *AXAF-S* (Zhang *et al.* 1990)) the important temperature diagnostic lines become blended, though we can still distinguish between ionization stages from Fe XX through Fe XXV.

Figure 9 shows simulations of observations on Capella and Algol (peak flare) (source parameters from Table 1) with the calorimeter on *AXAF* (with resolution $\Delta E = 7$ eV and effective area $\sim$ 170 cm^2, Linsky 1990) for different wavelength binnings. In the case of the flare on Algol we can directly measure the very hot (70 MK) plasma component (cf. Mewe 1991a, Table 3) by the presence of the Lyman α features. We can distinguish in the spectrum around 1.78 Å the prominent Fe XXVI Ly

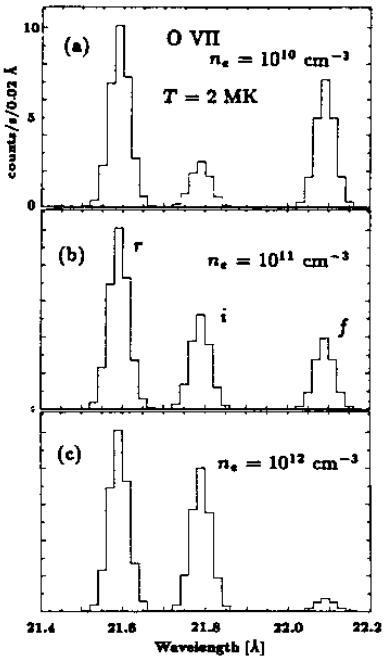

Figure 10: O VII triplet at 22 Å as observed with the *XMM* reflection grating spectrometer for temperature $T = 2$ MK, electron densities $n_e = 10^{10}$, 10^{11} and 10^{12} cm^{-3} (panels a,b,c), and reduced emission measure $\varepsilon/d^2 = 10^{52}$ cm^{-3} pc^{-2} (d is source distance). The spectra are binned in 0.02 Å bins. Symbols r, i, f indicate the resonance, intercombination, and forbidden line, respectively.

$\alpha 1$ and $\alpha 2$ components at wavelengths of 1.778 Å and 1.783 Å, respectively, and also (at a binning of 0.05 Å) an indication of the strongest Fe XXV (J) dielectronic recombination satellite line at 1.792 Å. The relatively low temperature (25 MK) of Capella and the poor statistics impede to measure here separately significant lines in the spectrum. But at longer wavelengths very good diagnostics can be made in both spectra from the Fe XXV w, x, y, and z lines at 1.851 Å, 1.856 Å, 1.860 Å, and 1.869 Å, respectively. Moreover the strong blend of Fe XXIII (and XXIV) dielectronic recombination satellite lines between 1.872–1.877 Å can be distinguished in the Capella spectrum. With the bolometer we begin to approach the resolution of a Bragg crystal spectrometer but with a four times bigger area.

5.3 Diagnostics of plasma parameters

High-resolution spectroscopy will permit the diagnostics of a variety of coronal plasma parameters such as temperature, ionization balance, emission measure, abundances, densities, and velocities (for details cf. Mewe 1991a).

The wavelength band 1–140 Å contains a multitude of prominent lines from nearly all ionization stages

Table 3: **Selected lines and continuum bands for temperature and abundance analysis***

Ion	Trans.	λ (Å)	T_m (MK)	Ion	Trans.	λ (Å)	T_m (MK)
Ca XIX	He4	3.177	40	Si X	B6a	50.530	1.6
S XVI	H1	4.729	20	S VII	Ne5	60.610	0.5
Si XIV	H1	6.182	20	Fe XII	P2b	80.020	1.6
Fe XXIV	Li2	7.987	18	Fe IX	A1a	82.425	1
Mg XII	H1	8.421	10	Mg VII	C4	83.964	0.8
Mg XI	He4	9.170	6	Fe XVIII	F4a	93.930	5
Fe XVIII	F2d	14.204	6	Fe IX	A2	103.564	1
Fe XVII	Ne5	15.012	4	Fe XIX	O6a	108.370	6
O VIII	H1	18.969	3	Ni XXV	Be13a	117.950	16
O VII	He4	21.600	2	Ne VI	B6a	122.490	0.5
C VI	H1	33.736	1.3	O VI	Li3	129.870	0.3
C V	He4	40.270	1	Fe VIII	K4a	131.247	0.8
Si XII	Li6b	44.165	2	Fe XXIII	Be13a	132.840	13
Fe XVI	Na6	50.400	2.5	Fe XXII	B12a	135.780	10
continuum band		3.2–3.4	(100)	continuum band		90–91	(3)
continuum band		4.4–4.6	(100)	continuum band		124–126	(2)
continuum band		7.5–7.65	(50)	continuum band		138–140	(2)

* These lines and continuum bands are relatively free from blends. For notation of transitions see Mewe *et al.* (1985a, their Tables I and III): e.g., He4 (or H1) is the resonance line of the He- (or H-)like isoelectronic sequence. T_m is the temperature of maximum intensity. Data are selected from Mewe *et al.* (1991).

Table 4: **Selected lines for density diagnostics***

Ion	Trans.	λ (Å)	T_m (MK)	Range	Ion	Trans.	λ (Å)	T_m (MK)	Range
Si XIII	He5	6.69	9	14–17	Ne IX	He5	13.55	4	12–15
Si XIII	He6	6.74			Ne IX	He6	13.70		
Mg XI	He5	9.23	6	13–16	O VII	He5	21.80	2	10–13
Mg XI	He6	9.31			O VII	He6	22.10		
Fe XXIII	Be6b	11.46	13	11–15	C V	He5	40.73	1	8–11
Fe XXII	B6c	11.93	11	11–15	C V	He6	41.47		
Fe XXI	C4a	12.29	9	11–15	Fe XIX	O6a	108.37	6	10–15
Fe XXI	C4d	12.46		10–14	Fe XXI	C6a	128.73		10–15

* For notation of transitions see Mewe *et al.* (1985a). T_m is temperature of maximum intensity. Range 14–17: $n_e = 10^{14}$–10^{17} cm^{-3}, etc. Data are selected from Mewe *et al.* (1991).

of cosmically abundant elements, including the K-shell transitions of carbon through iron, and the L-shell transitions from silicon through iron. If suitably resolved these lines are powerful diagnostics of plasma parameters because the line strengths are generally very sensitive to the electron temperature, the elemental abundances, and in some cases to the electron density. In certain circumstances (e.g. transient plasmas) the line intensities are dependent on deviations from the ionization equilibrium or to deviations from Maxwellian electron energy distributions (e.g. Raymond 1988, Mewe 1990a).

5.3.1 Electron temperature diagnostics

The soft X-ray spectrum depends sensitively on the ionization structure throughout the temperature range $T = 0.1$–100 MK, so that the mere detection of many lines will provide an accurate "thermometer" for the source emission region. Figures 4–9 clearly show that the improved spectral resolution of future spectrometers on *AXAF* and *XMM* will allow to resolve virtually all important spectral lines yielding the possibility to resolve the coronal temperature and ionization structure in more detail. Table 3 presents a selection from Mewe *et al.* (1991) (cf. also Mewe 1991a) of spectral lines from various elements in different ionization stages that are well suited as temperature diagnostics.

The electron temperature T can be diagnosed from the intensity ratio of two collisionally excited lines from different ions of the same element assuming coronal stationary ionization equilibrium, but this technique is limited by the assumption of ionization equilibrium and assumes an *isothermal* plasma. In situations in which deviations from ionization equilibrium occur one can get rid of this constraint by using the ratio of two lines depending on the same ionization stage, but differently depending on temperature, e.g. two collisionally excited lines with different excitation energies such as the Lyman α and β lines. Alternatively, one can measure the ratio of lines at nearly the same wavelength for which the excitation functions have a different dependence on T, e.g. in the helium-like $2 \rightarrow 1$ triplet. This consists of a resonance (r) $2^1P \rightarrow 1^1S$ line, a forbidden (f) $2^3S \rightarrow 1^1S$ line and an intercombination (i) $2^3P \rightarrow 1^1S$ line (summed over two close components). The intensity ratio $r/(i+f)$ varies with electron temperature.

Another possibility is to use the intensity ratio of the collisionally excited resonance line and a nearby dielectronic recombination satellite line (Gabriel 1972). This ratio goes as $T\ \exp[(E_s - E_0)/kT]$ (where E_s is the satellite energy above the ground state of the recombining ion and E_0 is the excitation energy of the resonance line; e.g. $E_0 = 6.7$ keV for the helium-like Fe XXV resonance line and $E_s = 4.7$ keV for the Fe XXIV satellite line). The latter technique (Gabriel 1972) has been widely used to derive Solar flare temperatures from very high-resolution X-ray spectra of the K-shell transition blends of helium-like Ca XIX (3 Å) and Fe XXV (1.9 Å) (cf. also discussion by Mewe (1988)). The helium-like triplets with their satellites provide a very valuable diagnostics for electron temperature, emission measure, abundances, and ionization balance.

5.3.2 Electron density diagnostics

From spectral fits to the line and/or continuum emission one can determine the emission measure, but one needs to know the electron density to determine the emitting volume V, hence the product Lf of loop length and filling factor, i.e. the fraction of the apparent volume that actually emits the X-rays (e.g. f may be much less than unity if the emitting volume viewed suffers a high degree of filamentation). If applied to stellar coronae, density observations (e.g. Mewe 1991a), possibly repeated at appropriate phases within the stellar rotation period, will allow us to constrain the coronal

dimensions in single stars and non-eclipsing binaries, while this is currently only rarely possible for eclipsing binaries.

Electron densities can be measured using density-sensitive spectral lines originating from metastable levels or using innershell excitation satellites to resonance lines (for reviews, e.g. Feldman 1981, Mewe 1988). In the first case the helium-like $2 \rightarrow 1$ triplet system lines are particularly important (Gabriel and Jordan 1969, 1972; Pradhan and Shull 1981; Pradhan 1982, 1985; Mewe et al. 1985a). The helium-like intensity ratio f/i varies with electron density due to the collisional coupling between the metastable 2^3S upper level of the forbidden line and the 2^3P upper level of the intercombination line. It does not depend on the model because its density dependence is determined only by the collisonal coupling between the two upper line levels. The f/i line intensity ratio of helium-like ions from carbon through magnesium in the wavelength region 9–42 Å can be used to diagnose coronal plasmas in the density range $n_e = 10^8$–10^{13} cm^{-3} and corresponding temperature range $T \sim$ 1–6 MK. Figure 10 shows the O VII triplet as observed with the *XMM* reflection grating spectrometer for a coronal plasma with a temperature $T = 2$ MK.

For density diagnostics in active late-type stars one must observe lines formed at temperatures around $T \sim 10$ MK. For this purpose Mewe et al. (1985a, 1991) have considered many density-sensitive lines in the Fe L-shell complex, i.e. 2ℓ–$\geq 3\ell'$ transitions from ions Fe XVII–XXIV (and some corresponding nickel lines from Ni XXI–XXIV) covering the wavelength region 7–13 Å, lines between 90–140 Å from 2ℓ–$2\ell'$ transitions in Fe XVIII–XXIII, and lines between 170–275 Å from 3ℓ–$3\ell'$ transitions in Fe IX–XIV ions. The density dependence is because the upper line level can be excited from various sublevels within the ground state which become collisionally coupled at increasing densities (the same holds for the satellite lines). The Fe and Ni lines can be used as tools for diagnosing plasmas in the density range 10^{10}–10^{15} cm^{-3} and temperature range $\sim$ 0.5–15 MK.

A selection of a number of density-sensitive lines is presented in Table 4 (from Mewe 1991a). The latter author has also discussed the limited possibilities for density diagnostics in Fe K-shell spectra (his Figure 11).

5.3.3 Differential emission measure (DEM) modelling

In many sources the X-ray spectrum will not be a unique function of one single temperature, but instead will be determined by a distribution in temperature across the emission region. Then the observed spectra can be described in terms of a differential emission measure (DEM) distribution, which is defined as follows. The observed spectral flux $f(\lambda)$ (counts s^{-1}) measured at Earth by a given instrument at wavelength λ can be expressed as:

$$f(\lambda) = \frac{1}{4\pi d^2} \oint F(\lambda,T) n_e^2 dV = \frac{1}{4\pi d^2} \int F(\lambda,T)\varphi(T)\, dT \equiv \frac{1}{4\pi d^2} \int F(\lambda,T) T\varphi(T)\, d\ln T, \qquad (3)$$

where $F(\lambda,T)$ is the spectral emissivity (counts cm^5 s^{-1}) for the line plus continuum emission as a function of temperature T at wavelength λ, convolved with the instrument response function; d (cm) is the distance to the source and $\varphi(T) = n_e^2 \frac{dV}{dT}$ (cm^{-3} K^{-1}) is the differential emission measure, $n_e(T)$ is the electron density (cm^{-3}) and V the plasma volume (cm^3). Note that the total emission measure is given by $EM = \oint n_e^2 dV = \int T\varphi(T) d\ln T$. For graphic representations of the DEM we will use $T\varphi(T)\Delta\ln(T)$.

The differential emission measure distribution can be derived from the observed spectrum by decon-

volving $\varphi(T)$ from the measured spectral intensities, using known emission functions for the individual wavelength bins. For this deconvolution we can apply an iterative technique which uses an initial form for the differential emission measure, $\varphi_0(T)$, to calculate theoretical line intensities. The comparison of observed and theoretical line intensities yields a new $\varphi_1(T)$. Subsequent iterations are performed to minimize the value of χ^2, given by

$$\chi^2 = \sum_{j=1}^{N} \frac{(f_{\rm O}(\lambda_j) - f_{\rm C}(\lambda_j))^2}{\sigma^2(\lambda_j)}, \tag{4}$$

where $f_{\rm O}(\lambda_j)$ and $f_{\rm C}(\lambda_j)$ are the observed and computed intensities in N intervals at wavelengths λ_j, $\sigma(\lambda_j)$ is the statistical uncertainty in the observed count rate. We use the Withbroe-Sylwester iteration scheme (originally proposed by Withbroe (1975), and modified by Sylwester, Schrijver, and Mewe (1980)) for successive approximations of the differential emission measure distribution $\varphi_i(T)$ (see also Fludra and Sylwester 1986):

$$\varphi_{i+1}(T) = \varphi_i(T) \frac{\sum_{j=1}^{N} W_j(T) f_{\rm O}(\lambda_j)/f_{\rm C}(\lambda_j)}{\sum_{j=1}^{N} W_j(T)}. \tag{5}$$

Sylwester, Schrijver, and Mewe (1980) derived a semi-empirical expression for the weighting function $W_j(T)$, which takes into account the uncertainties in the measurements. N is the total number of bins of the fitted spectrum. The method places no restrictions on the functional form of the differential emission measure distribution, although the final result is subject to an implicit smoothing because spectra with neighbouring values of T are more or less alike. From an analysis of the library of spectra in terms of the mutual correlations it can be shown that the widths in temperature of the correlation functions determine the "temperature resolution", i.e. the scale on which we can extract detail of the DEM distribution. The described technique is formulated to exclude *a priori* negative values for the emission measure.

For comparison we have sometimes also used a second approach – the Polynomial (P) method – which assumes that the shape of $\varphi(T)$ can be approximated by the exponential of a polynomial given by $\varphi(T) = \alpha \exp[\omega(T)]$, where α is a normalization constant and $\omega(T)$ is a polynomial function of temperature. A detailed DEM analysis has been performed on the *EXOSAT* transmission grating spectra (TGS) of several late-type stars by Lemen et al. (1989) and Schrijver et al. (1989) to constrain the basic properties of stellar magnetic loops, and by Mewe et al. (1991) to extract the DEM for simulated spectra for the *AXAF*-LETGS (see §6.1.3).

The DEM modelling can be applied equally well to investigate the temperature structure of other types of optically thin plasmas such as SNRs and cooling flows in clusters of galaxies so that in many cases this analysis will be the primary handle one can use to test models for the physics of the source emitting region.

5.3.4 Elemental abundance diagnostics

In both coronal equilibrium and nonequilibrium situations, ions of different elements which have similar ionization potentials usually coexist in close proximity. Thus the ratios of the prominent emission lines from ions of different elements yield in a relatively model-independent way elemental abundances. By using a suitable set of lines from different ionization stages from one given element, e.g. iron, we

can determine the temperature distribution by fitting the line intensities. Then by selecting suitable lines from different elements, relative elemental abundances can be determined and by determining intensity ratios of lines to neighbouring, unblended continuum bands, the absolute abundances can also be derived. We give a selection of lines for abundance diagnostics in the soft X-ray wavelength range 1–140 Å covered by the instruments on *AXAF* (from Mewe *et al.* 1991, Mewe 1991a).

5.3.5 Velocity diagnostics

In particular spectroscopy with high spectral resolution ($\Delta\lambda \simeq 0.05$ Å) at longer wavelengths ($\gtrsim$ 100 Å) with *AXAF*-LETGS will permit for the first time detailed studies of spectral line profiles in the X-ray region (cf. Mewe *et al.* 1991, Mewe 1992b). This may provide direct measurements of wind expansion velocities of stellar coronae, flow velocities along magnetic loops in stellar active regions or flares, orbital velocities in X-ray binaries, etc. The Doppler shift caused by the orbital motions in close binaries may suffice in some cases to determine the relative activity level of the binary components. Observations at the two quadratures yield the intensities of the two components separately, hence indicate which star is the stronger X-ray source or whether the X-rays are emitted by the corona of both stars or perhaps by a common corona.

5.3.6 Temporal variability

An important diagnostic of stellar coronal activity is temporal variability of the coronal X-ray emission. For example, in the case of flares the study of light curves (cooling times), in combination with the determination of temperature T and emission measure EM will yield estimates of plasma volume, loop length and density n_e (e.g. Van den Oord *et al.* 1988, Van den Oord and Mewe 1989, Mewe *et al.* 1989). A useful diagnostic tool is provided by an analysis of the flare evolution in a T–DEM (or n_e) - diagram. From a comparison with scaling laws and numerical models one can derive the time-dependent flare energy release (e.g. Jakimiec *et al.* 1992, Cheng and Pallavicini 1991). Finally, in some cases it may be possible to quantify by selected line ratios emitted from a transient flaring plasma the extent of non-equilibrium as a function of time and thus, set limits on the plasma density (cf. §5.1.1 and Mewe *et al.* (1985b)).

6 Examples of various models

In the following we give several examples of calculated and observed spectra for optically thin plasmas such as stellar coronae and supernova remnants, for photo-ionized plasmas, and for optically thick plasmas or combinations thereof (e.g. active galactic nuclei).

6.1 Stellar coronae

In the case of a stellar corona a combination of quasi-statical loop models with temperatures close to the results from the multi-temperature fitting can be a fruitful approach to describe the observations (e.g. Schrijver *et al.* 1989).

6.1.1 Static loop models and scaling laws

The simplest model consistent with the observations is that of a quasi-static loop in which the energy deposited into each volume element is balanced by the energy lost through radiation and conduction. The magnetic pressure dominates the gas pressure, causing the heat conduction to occur predominately along the magnetic field lines. Mass flows in the loop and drifts across magnetic field lines are neglected. The plasma is described by a one-fluid model. Rosner, Tucker, and Vaiana 1978 (hereafter **RTV**) derived analytical solutions to simplified versions of the equations of energy balance and hydrostatic equilibrium, neglecting gravity and assuming uniform cross section, heating and pressure throughout the loop, a monotonic increase of temperature with height, and a radiative loss function $\propto T^{-1/2}$. This model predicts a simple scaling law relating loop half-length, L (cm), maximum temperature, T_m (K), and pressure, p (dyne cm^{-2}): $T_m \simeq 1400(pL)^{1/3}$ (cf. also Mewe 1991b).

A variety of Solar loops ranging from small bright points to active region loops and large-scale structures can be modelled by this scaling law. There is an overall agreement, within a factor of two, between observed (L_{obs}) and calculated (L_{calc}) loop lengths, with the exception of compact flare loops for which $L_{calc} \gg L_{obs}$.

While it has not yet been possible to derive the differential emission measure distribution for individual loops, careful emission measure analyses were performed for the integrated soft X-ray and EUV emission of active regions using *OSO*-4,6 and *SKYLAB* data (for references see Mewe (1991b)). Extensive analysis of the data (e.g. Pallavicini *et al.* 1981) revealed satisfactory agreement with existing static loop models for the upper portion ($T \gtrsim 0.5$ MK) of loop structures ranging from compact, dense active-region loops to more extended, tenuous loops interconnecting active regions. Loop lengths (cm), pressures (dyne cm^{-2}) and temperatures (MK) range from $L \sim 3\ 10^9$, $p \sim 5$ and $T \sim 3.5$ for compact active-region loops through $L \sim 9\ 10^9$, $p \sim 1.5$, $T \sim 3.3$ for extended active-region loops (matching the average of a solar active region), to $L \sim 2\ 10^{10}$, $p \sim 0.2$, $T \sim 2$ for large-scale loops which interconnect active regions, or which are over quiet regions; flaring or post-flare loop plasmas have much higher temperatures ($\gtrsim 10$ MK) and pressures ($\gtrsim 10^3$ dyne cm^{-2}) (e.g. Priest 1978 and Mewe 1991b). Recently Mewe (1991b) has reviewed the X-ray observations in the context of the physics of Solar and stellar coronal loops.

6.1.2 Modelling of coronal loops on cool stars

For late-type stars with convective envelopes the solar analogue appears to be applicable, because the relationship between X-ray luminosity and stellar rotation suggests that surface magnetic fields - generated by a dynamo mechanism - are responsible for the heating of a coronal plasma with temperatures ranging from one to several tens of millions Kelvin. Although the dependence of stellar magnetic activity on rotation rate is widely accepted, the precise functional relationship is not yet known. It appears to depend on additional parameters like effective stellar temperature and surface gravity. The majority of late-type coronae is thought to be solar-like in the sense that the same physical processes as in the Sun are likely to be relevant for the formation and heating of coronae, though in many cases the level of X-ray activity can be orders of magnitude higher than on the Sun (e.g. Linsky 1985).

Although the detailed spatial structure of stellar coronae is not yet known - except for a few cases in which eclipsing binaries were studied - it is widely assumed that by analogy with the Sun, the tenuous, hot coronal plasmas emitting copiously X- and EUV-rays are for a large part confined in loop-like structures connecting opposite magnetic polarities observed in the photosphere and are heated by

magnetohydrodynamic processes.

The imaging proportional counter (IPC) on the *EINSTEIN* Observatory has observed soft X-ray emission of the coronae of many late-type stars. The crude spectral resolution ($\lambda/\Delta\lambda \sim 1$) gives some indication of the coronal X-ray temperature T_X but it does not permit a detailed analysis of the differential emission measure structure. Single- (or two-)temperature fits give usually an adequate description of the observed IPC-spectra. The data show that T_X increases markedly with activity and differs strongly between giants and dwarfs of moderate activity. Two "branches" can be identified: a low-temperature branch containing only dwarfs and a high-temperature branch containing mainly giants; at high temperatures the two branches meet (Schrijver et al. 1984). These authors have discussed the IPC data in terms of the static loop model (i.e. the scaling law). Though interesting conclusions on characteristic loop size and geometry and heating rates could be derived from all these data (cf. also Fig. 1 from Mewe (1991b)), the interpretation of such single-temperature fits is difficult without any further information on the temperature structure of stellar coronae. Detailed modelling is difficult because the IPC had a rather limited wavelength range and a poor spectral resolution. For an unambiguous interpretation we need observations with a better spectral resolution such as for example have been made with the spectrometers on *EINSTEIN* and *EXOSAT* which have shown that data of even modest spectral resolution ($\lambda/\Delta\lambda = 10$–$100$) permit the identification of coronal material at different temperatures whose existence may relate to a range of possible magnetic loop structures in the hot outer atmospheres of these stars.

6.1.3 Spectral modelling in terms of DEM and loop models

From multi-temperature fits to the entire spectrum we derive the DEM distribution and may assess contributions to the coronal energy balance.

With the transmission grating spectrometer (TGS) on *EXOSAT* spectra with a resolution $\Delta\lambda \sim 3$ Å have been obtained between 5–200 Å for three late-type stars Capella, σ^2 CrB, and Procyon (cf. Brinkman et al. 1985; Schrijver 1985; Mewe et al. 1986b; Lemen et al. 1989; Schrijver et al. 1989). A detailed DEM analysis has been performed on the TGS spectra by Lemen *et al.* (1989) and Schrijver *et al.* (1989) to constrain the basic properties of stellar magnetic loops. Lemen *et al.* (1989) have derived the DEM distributions from the spectra using two different algorithms: the Withbroe-Sylwester (WS) and the Polynomial (P) method. The results for the differential emission measure distribution are plotted in the right panels of Figure 16 in the form of $T\varphi(T)$ per interval $\Delta\ln(T) = 0.081$, together with a comparison in the left panels between the corresponding observed and best-fit spectra. The characteristic features of the DEM distributions are remarkably similar for the spectra of Capella and σ^2 CrB: a very steep increase with temperature up to 3 MK, followed by a "depression" around 10 MK (demonstrated to be real and not an artifact of the analysis method), and another increase towards $T \approx 20$ MK. The differences between the results from the two algorithms are an indication of the uncertainties in determining $T\varphi(T)$. The resulting $T\varphi(T)$ for the two different algorithms are in good agreement for temperatures between 2 and 20 MK, for which pronounced spectral lines are available in the spectra. Large discrepancies between the two $T\varphi(T)$ curves for each of the stars occur at $T < 3$ MK (Figure 11). The spectral range between 160 – 200 Å contains lines that are sensitive to temperatures down to 0.5 MK, but the observed intensities are small. Thus, the differences at low temperatures between the DEM curves from the two different algorithms are not significant. The models are not well constrained for $T \gtrsim 20$ MK due to the lack of strong spectral lines formed at these high temperatures and this is reflected in the disagreement of the two models in that region (cf. Figure 11). The DEM distribution derived for Procyon is uncertain because of the

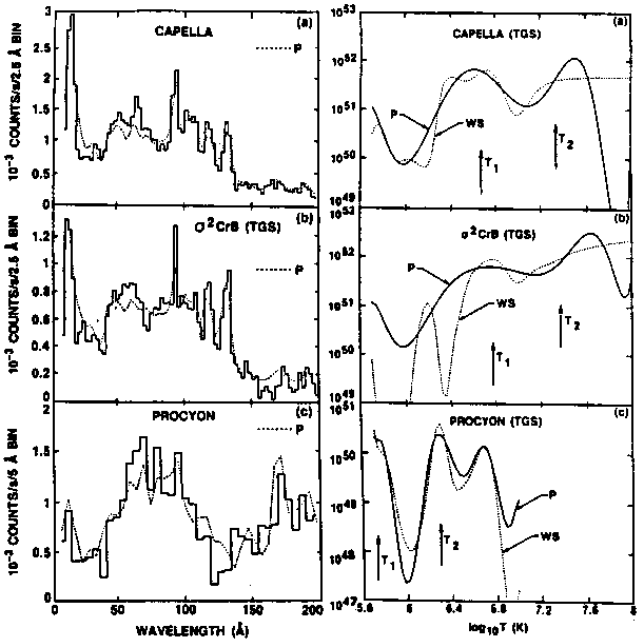

Figure 11: *EXOSAT* 500 l/mm TGS spectra of (a) Capella, (b) σ^2 CrB , and (c) Procyon compared with a polynomial best-fit spectrum (left panels). Corresponding curves for DEM $\equiv T\varphi(T)\Delta\ln(T)$ with $\Delta\ln(T)$=0.081 for the same sources (right panels) and for different methods (Polynomial (P) and Withbroe-Sylwester (WS)). Arrows in each panel mark the results of two-temperature fits. (Adapted from Figs. 4 and 6 of Lemen *et al.* (1989); note that we have corrected an error in the DEM figure for Procyon by dividing the scale by a factor of 100).

poor signal-to-noise ratio of the spectrum. A relatively strong contribution is suggested from plasma at $T \sim 0.6$ MK and at T in the range between 2 and 6 MK (Schmitt *et al.* (1985) also find the latter T component in the *EINSTEIN-IPC* spectrum).

The existence of three dominant temperatures in the coronae of cool stars may contain information on the stability of the corresponding loops. Lemen *et al.* (1989) note that these temperatures correspond with temperature intervals where the radiative loss function increases with T. If radiation is the dominant cooling mechanism, the loop apex temperatures may tend to reach values for which the loop plasma is relatively stable against heating perturbations.

Mewe et al. (1986b) and Schrijver and Mewe (1986) did a first attempt to model the *EXOSAT* spectra in terms of a differential emission measure (DEM) distribution and compared the results with computed spectra using the RTV loop model. They show that the spectra observed for Capella and σ^2 CrB are incompatible with the RTV model for static loops of constant cross section: The RTV model predicts much too strong radiation beyond 140 Å caused by the emission from Fe VIII-XI formed

around 1 MK. One possibility is that the cross-section of the loop increases with height so that most of the matter in the loop is at a high temperature, and thus the spectrum appears isothermal. On the basis of a detailed DEM analysis Lemen et al. (1989) confirm that the steep increase of the DEM with temperature from below 3 MK for Capella and σ^2 CrB is incompatible with the RTV model and that the emission of the corona of each of the cool stars observed by the TGS is dominated by plasma in two relatively narrow temperature intervals: 5 MK and 25 MK for Capella and σ^2 CrB, and 0.6 MK and $\sim$ 2 MK for Procyon. These doubly peaked DEM distributions suggest a model corona comprising two distinct ensembles of quasi-static magnetic loops with maximum temperatures around the dominant temperatures given above and with the cool ($T \sim 5$ MK or ~ 0.6 MK, respectively) loops probably expanding with increasing height over the photosphere. To test this hypothesis Schrijver et al. (1989) performed a two-component analysis of the *EXOSAT* spectra using computed loop spectra covering a range of apex temperatures T_m and expansion factors Γ (= ratio of loop cross section at apex to cross section at footpoint in the upper chromosphere where $T = 3\ 10^4$ K). The model spectra were generated with a revised computer code originally developed by Vesecky et al. (1979), using the spectral model of Mewe et al. (1985a). The fits for Capella and σ^2 CrB suggest that the cool (5 MK) component originates in loops expanding significantly with height ($\Gamma \gtrsim 5$). This is in fact indirectly observed on the Sun: coronal condensations over magnetic bipolar regions have a projected area roughly an order of magnitude larger than the area of the underlying photospheric plage (e.g. Schrijver 1987). However, recent results with the soft X-ray telescope on *YOHKOH* seem to contradict this because it was found that the majority of loops have nearly constant cross sections along their lengths, rather than expanding with height (Lemen 1992).

Mewe *et al.* (1991) have applied a DEM analysis on simulated *AXAF*-LETGS spectra as a test to investigate the possibilities to extract the DEM from such observations. In Figure 12 we present their results for a two-component loop fitting of an *AXAF*-LETGS spectrum simulated for the model of a Capella-like X-ray source. For the two loops were taken the following parameters: apex temperatures of 5 and 24.5 MK, apex cross sectional areas of 60 and 0.8 ($\times 10^{21}$ cm^2) and geometric expansion factors Γ (= area ratio top/bottom) of 20 and 2. A larger number of iteration steps limits the high-temperature tail, but the low-temperature structure is only crudely approximated because of the lack of strong spectral lines that may constrain the DEM distribution.

6.2 Model of a Supernova Remnant

An important class of thin X-ray sources are the remnants of supernova explosions, which play a dominant role in the heating and the replenishment (hence the enrichment by heavy elements) of matter in the surrounding interstellar medium. Supernova explosions, dramatic events in themselves, have also profound and long lasting effects on the appearance and future evolution of the galaxies in which they occur. Following a stellar explosion a substantial fraction of the star's mass is ejected at high velocity into the surrounding interstellar medium and the visible manifestations of such an event are collectively described by the term supernova remnant (SNR). For young remnants (i.e. those with age $\lesssim 10^4$ years) the associated high-temperature plasma is mostly comprised of ejected material, whereas for the old remnants the plasma results from the ambient interstellar gas that has been heated by the passage of the shock wave from the explosion. In either case, plasma temperatures are in the range above 1 MK and hence observations of spectrally resolved X-ray emission lines provide the most useful information about this hot gas.

A SNR is a typical example of a more involved plasma model in which the transient nature of the plasma and its spatial structure must be taken into account for a proper interpretation of the observed

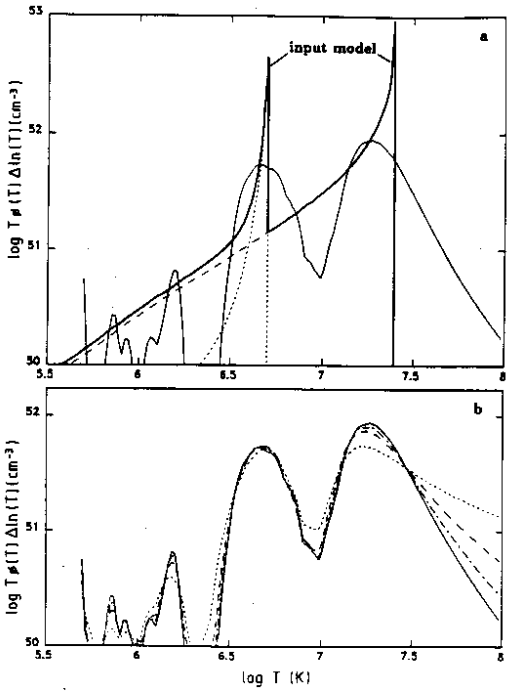

Figure 12: Results of two-component loop fitting of *AXAF*-LETGS spectra for a Capella-like X-ray source (for parameters, see text). The input DEM model based on two loop components (a) is compared to the DEM resulting from an analysis of the spectrum associated with the input DEM model for exposure time $t_{exp} = 10^4$ s and for 150, 300, 450, and 600 iteration steps and noise added (dotted, dashed, dashed-dotted, and solid curves, resp.) in (b). The DEM curve for 600 steps is superimposed as a thin solid line on the input model (heavy solid line) in (a) (from Mewe *et al.* 1991).

X-ray spectrum. The evolution of a SNR can be described by a blast wave (originating from an initial point explosion) propagating outwardly in the surrounding medium, forming an optically thin, shock-heated plasma that emits X-ray radiation. In the early phase, when the SNR is in the transition between free expansion and the adiabatic phase, the deceleration of the ejected material by the shocked ambient medium causes the development of a reverse shock propagating inwardly relative to a co-moving reference frame.

In order to generate a model SNR model the following steps can be distinguished (e.g. Kaastra and Jansen 1992): First, the hydrodynamical model is calculated: the distribution of density, velocity and temperature as a function of position and time. In the case in which radiative losses are negligible compared to other terms in the energy balance we can assume that the radiation mechanisms are decoupled from the hydrodynamics. Given the hydrodynamical model, the ion densities are evaluated by integrating the electron temperature and electron density dependent equations for the ionization balance over time. Then we compute the X-ray spectrum for the known set of ion concentrations for each position in the SNR. Finally, we include Doppler shifts due to the plasma motion and project

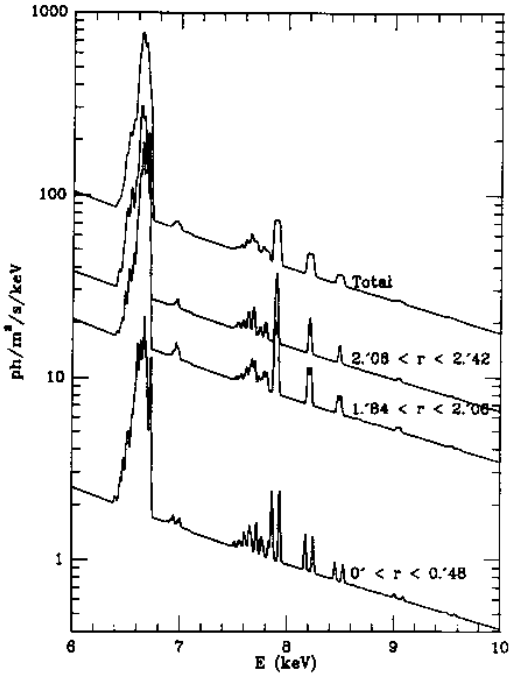

Figure 13: Simulated X-ray spectra of the Fe K and Ni K complexes integrated over different zones of a supernova remnant for the Chevalier model (from Kaastra and Jansen 1992).

the spectrum onto the sky and integrate it over the relevant area of the sky. Kaastra and Jansen (1992) have used several models to describe the hydrodynamics. In Figure 13 we show their results for the spectrum near the Fe-K and Ni-K line complexes in the region 6–10 keV, calculated for the model of Chevalier for an adiabatic remnant containing a reverse shock. The spectral resolution is 0.2 %, easily obtainable by the future missions *AXAF* and *XMM*. The total Fe Kα complex (6.6 keV) is rather featureless due to the Doppler broadening caused by the radial expansion of the remnant and the integration over the whole remnant. However, if we can resolve the SNR in the observations spatially in more detail the spectra will show up more spectral details, e.g. the spectra taken from two annuli around $2'$ and from the central part within $0.5'$, where the Doppler doubling of lines due to the radial expansion of 1200 km/s is clearly visible.

6.3 Clusters of galaxies

Clusters of galaxies are prominent X-ray sources due to the presence of hot intracluster gas. The discovery of iron line emission at $\sim$ 6.7 keV has demonstrated that such intracluster gas must have been processed in stars within the galaxies, since it is enriched with heavy elements. An accurate determination of the temperature of this gas (10-100 MK) provides the opportunity to measure the

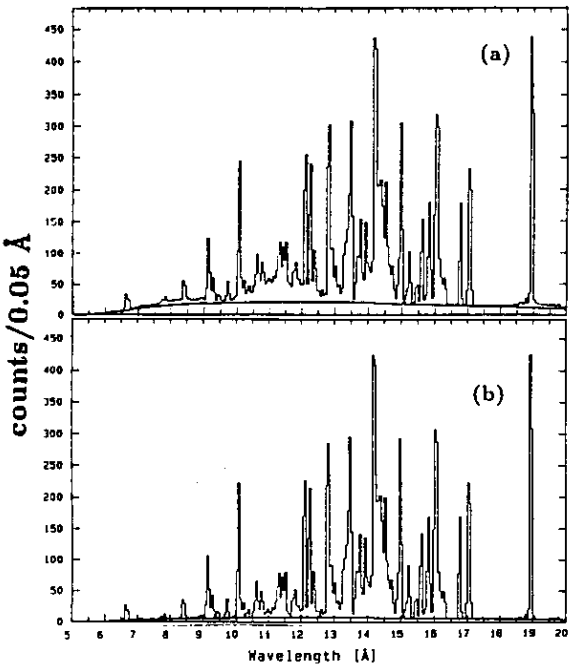

Figure 14: Two-temperature spectrum of the cooling flow onto M87 in the Virgo cluster, folded through the response of the *XMM*-RGS for an observation time of 10^4 s. Top panel (a) shows the total spectrum of cooling flow (T_1=7 MK) and hot cluster gas (T_2=20 MK), bottom panel (b) shows the (dominant) contribution of the cooling flow only. Interstellar hydrogen column density $N_H = 10^{21}$ cm^{-2}. At the distance of 20 Mpc the cooling flow can be considered as a point source, but the finite extent of the hot gas component appreciably degrades the instrumental resolution and efficiency.

gravitational cluster potential, since the gas must be close to hydrostatic equilibrium. This gives an indication of the "hidden" mass in the cluster which appears to be a common constituent of our Universe. The gas density within the core of a cluster is generally so high that radiative cooling is important and an inflow of gas takes place onto the central galaxy. The mass flow of the cooling gas is estimated to reach sometimes very large values of up to 400 solar masses per year, which implies that the total accumulation of matter can be comparable to the mass ($10^{12} M_\odot$) of a whole large galaxy. The simple presence or absence of certain spectral lines defines the temperature distribution in the source. Figure 14 shows a simulated spectrum observed by the Reflection Grating Spectrometer (RGS) on *XMM* of the cooling flow onto the massive galaxy M87 at the core of the Virgo cluster. A simple two-temperature model has been used (parameters from Lea *et al.* (1982)). With a relatively short (10^4 s) exposure the emission lines of the cooling flow are bright and well resolved, wheras the lines from the hot component are smeared out due to the finite source extent and give only a minor contribution.

6.4 Nebular model

The nebular model (e.g. Kallman and McCray 1982) is applicable to the case where gas is illuminated by a strong X-ray source and can be considered as the X-ray analogue of a planetary nebula. The gas may be the flow surrounding an accreting compact object, the stellar wind or atmosphere of a normal star, or interstellar medium in the line of sight. The temperature structure of the illuminated gas is established by a balance between heating (e.g. by photo-ionization, Compton heating, Auger electrons, charge transfer, and collisional de-excitation) and cooling (e.g. by radiative and dielectronic recombination, continuum bremsstrahlung (inverse Compton cooling), collisional ionization and excitation, and charge transfer). The ionization structure is determined by a balance between photo-ionization and radiative and dielectronic recombination, and charge transfer.

When the gas is optically thin in the photo-ionization continuum, the local radiation field is determined by geometrical dilution of the source spectrum. The local state of the gas at distance R from the central X-ray source can be described in terms of the scaling parameter $\xi = L/nR^2$ (L is source luminosity, n is local gas density) and when the gas is optically thick also in terms of $(Ln)^{1/2}$ which characterizes the continuum optical depth at a given value of ξ. The emerging X-ray spectrum will be dominated by absorption edges and consists of the central continuum with a low-energy cutoff due to photoabsorption and with emission lines due to recombination and fluorescence (in the latter case e.g. K-shell lines from ions with sometimes nearly stripped L-shells), typically near the absorption cutoff.

It may be instructive to contrast the nebular model with the coronal model. In the latter model the mechanism for heating the gas is not specified, but the heat input is coupled directly to the ions and free electrons. The parameters characterizing the coronal model are (electron) temperature, element abundances, and emission measure. At a given temperature only one or two ionization stages of a given element are abundant. In the nebular model the temperature of the gas is not a free parameter, but instead is determined by absorption and emission of radiation in the gas. The elements are primarily ionized by innershell photoionization. As a result a wider range of ionization stages of a given element can simultaneously occur and the elements are more highly ionized ("overionized") at a given electron temperature than they would be in the coronal model.

X-ray photoionized plasmas can appreciably differ from collisionally ionized plasmas with similar ion concentrations. Because the photoionized plasma is *overionized* relative to the electron temperature, the excitations of important lines are dominated by recombination, photoexcitation, and cascades as opposed to collisional excitation and dielectronic recombination. This has a drastic effect on the emergent spectrum, as we illustrate in Figure 15 which has been derived from recent results by Liedahl *et al.* (1991) (see also Mewe 1990a). These authors have developed a useful diagnostic to distinguish between coronal and nebular models using high-resolution Fe L-shell spectra between 10–15 Å. They show that the $(3s-2p)/(3d-2p)$ line intensity ratios from Fe XVII–XIX ions in the Fe L-shell spectrum between 10–15 Å can be used to effectively discriminate between the coronal and the nebular models. The $3d$ lines are formed by electron collisional excitation from the ground state in a hot (5–10 MK) coronal plasma, whereas the $3s$ lines are formed by recombination in a much cooler (say 0.1 MK) photo-ionized plasma.

Another possibility to distinguish between nebular and coronal models is to measure the helium-like $2 \rightarrow 1$ triplet. This consists of a resonance (r) $2^1P \rightarrow 1^1S$ line, a forbidden (f) $2^3S \rightarrow 1^1S$ line and an intercombination (i) $2^3P \rightarrow 1^1S$ line. The f/i ratio varies with n_e and does not depend on the model because its density dependence is determined only by the collisional coupling between the two upper line levels, but the singlet/triplet ratio $R \equiv r/(i+f)$ (which can be used for coronal temperature diagnostics) does and can serve as an indication of the validity of the coronal model (see Mewe 1990a).

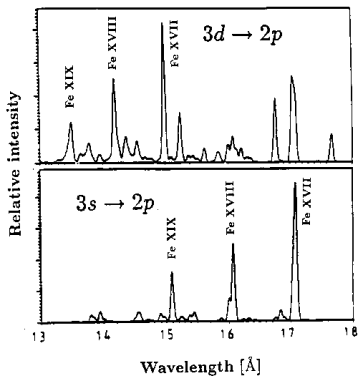

Figure 15:
Model spectra of Fe XVII–XIX from 13–18 Å with 0.052 Å resolution calculated by Liedahl *et al.* (1989). Both spectra are plotted on the same scale, wavelength in Å, intensity in arbitrary units. *Top:* Collisional equilibrium with $T = 5.75$ MK for the electron temperature. The strong lines at 13.5, 14.2, and 15.0 Å (from Fe XIX, XVIII, and XVII, respectively) are collisionally excited $3d$ lines. *Bottom:* Recombination-dominated spectrum at T=0.11 MK and ionization structure appropriate to an X-ray photoionized nebula. The prominent lines at 15, 16, and 17 Å (from Fe XIX, XVIII, and XVII) are all recombination-cascade-populated $3s$ lines, which cannot be excited by electron collisions at this low electron temperature. The electron density is in each case 10^{11} cm^{-3}.

E.g. for the O VII triplet $R \sim 1$ for a coronal plasma (where the lines are excited by electron collisions from the ground) and $R \sim 3$ for a photo-ionized plasma (where population of the upper line level occurs through recombination, either directly or via cascades).

Though the lines produced by cascade following recombination are relatively insensitive to the temperature, the Fe L-shell spectra can provide a good temperature diagnostic by measuring the width of the recombination continua (Kahn and Liedahl 1991).

The relative line intensities detected in the photoionized case can be shown to be sensitive functions of the density and geometry of the emission regions and of the spectral shape of the photoionizing continuum.

Finally, it is instructive to show some results of recent calculations by Kaastra (1992b) for the case in which a power-law (E^{-2}) photon number spectrum of a central X-ray source is incident on a flat slab of thickness D ($=N_H/n_H$) homogeneously filled with gas of hydrogen column density N_H, electron temperature T, and volume density n_H. The gas composition is determined by cosmic abundances. To calculate the radiative transport an approximate escape factor method is used (e.g. Elitzur 1984, Ferland and Rees 1988). The combined spectrum consisting of transmitted radiation (shaded area), fluorescence radiation, and thermal radiation of temperature T is shown in Figure 16 for two models: 1. $N_H = 10^{23}$ cm^{-2}, $n_H = 1.5\ 10^{17}$ cm^{-3}, $T = 0.1$. keV; 2. N_H the same, $n_H = 10^{18}$ cm^{-3}, $T = 0.01$ keV. The incident power-law spectrum is shown as a dotted line. The line spectrum is a combination of fluorescence (e.g. Fe K feature near 6.4 keV) and thermal line and continuum radiation from the

slab.

6.5 Optically thick model

In very dense plasmas, e.g. in the inner regions of accretion flows on compact objects such as very hot white dwarfs in cataclysmic variables, neutron stars in hard X-ray binaries and the cores of AGNs, the source is optically thick to both continuum and line radiation. The spectrum will resemble, at very high optical depths, blackbody emission or a superposition of blackbody type spectra. At intermediate optical depths, the spectral formation is influenced by complicated radiation transfer effects. Discrete spectral structure can provide much information about the source. when Compton scattering plays a role (Ross 1979). Transfer through the scattering plasma will broaden and shift line profiles and alter the continuum distribution, depending on temperature and column density. Emission features observed from X-ray binaries lie in the wavelength region 9–20 Å and are probably from L-transitions from partially ionized iron atoms (Vrtilek *et al.* 1991). The spectral resolving power of the future spectrometers is sufficient to resolve the X-ray spectral features that are indicative of the nature of the Compton scattering processes as well as of the structure of the accretion disk corona or the magnetosphere of the neutron star.

6.5.1 Hot white dwarfs

An important class of objects to be studied at very soft X-rays are isolated hot white dwarfs with optically thick (in visible and UV) photospheric plasmas with effective temperatures in the range ~ 0.03–0.2 MK. At high gravity all hydrogen is pressure-ionized and the outer layers of the photosphere are transparent to the soft X-ray radiation of hotter and deeper layers which become optically thick to the X-rays. The shape of the X-ray spectra is very sensitive to photospheric parameters like effective temperature, gravity and element abundances (cf. Heise 1988). Trace amounts of highly ionized metals may produce a variety of absorption edges that can be detected in high-resolution X-ray spectra at long wavelengths and which allows one to accurately determine effective temperatures and element abundances for objects as hot DA and very hot DO white dwarf stars. For examples of simulations of various high-resolution X-ray spectra, see Mewe (1990b).

6.5.2 AGN model

Finally, we present an AGN model spectrum that exhibits a superpostion of various models. The most efficient energy sources known occur in active galactic nuclei. It is generally considered that accretion onto a supermassive black hole is the basic mechanism to power the central X-ray source. This process can be more than an order of magnitude more efficient in converting restmass to energy than is nuclear fusion. Detailed X-ray spectral studies are essential in understanding the accretion of matter onto such huge compact objects. Clearly this is of primary importance for testing the laws of physics under extreme conditions.

Current models of the X-ray emission of AGN distinguish between a hard X-ray power-law component, usually attributed to non-thermal radiation from the central source that is inverse-Compton scattered by very energetic electrons, and a soft excess above ~ 25 Å, associated with the hotter parts of the accretion disk and described by a modified blackbody spectrum or it may be thermal bremsstrahlung of tenuous gas, in both cases with temperatures in the range 0.3–1 MK. Hence the absence or presence

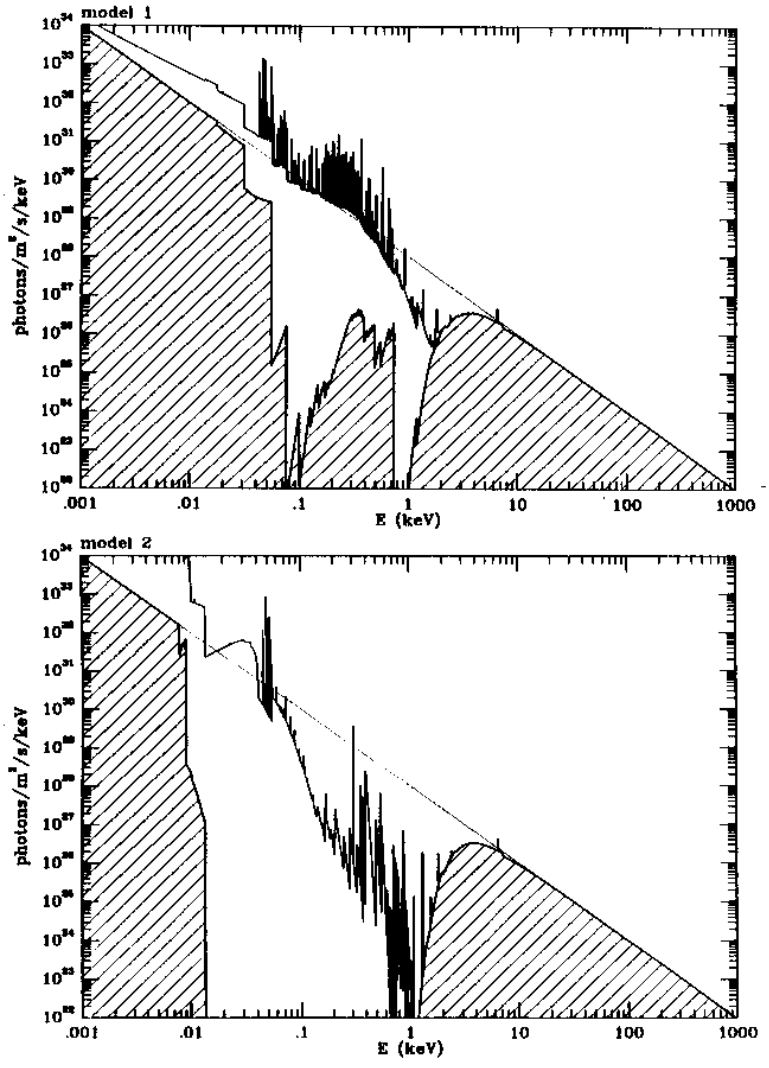

Figure 16: X-ray spectra calculated for the nebular model by Kaastra (1992b) for two models (for parameters, see text). The shaded area represents the incident power-law spectrum after transmittance through a slab of column density $N_H = 10^{23}$ cm^{-2} without reprocessing. The total spectrum contains also contributions from fluorescence and thermal radiation.

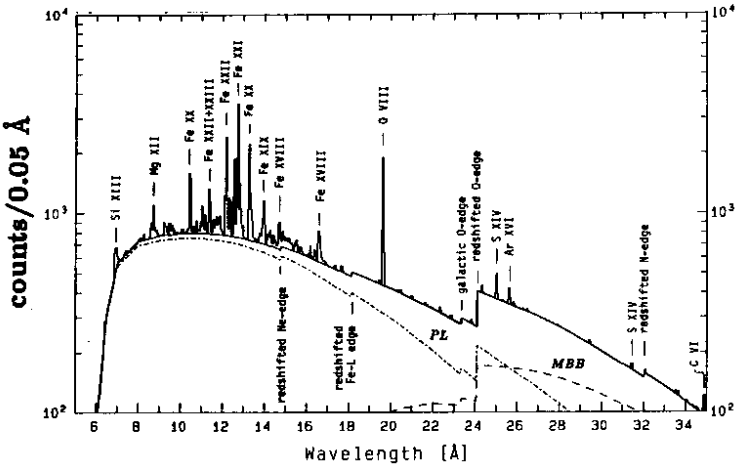

Figure 17: Simulated AGN spectrum as observed with the reflection spectrometer on *XMM* in 10^5 s. The contributions from power law (PL) and modified blackbody (MBB) spectra are also separately plotted (for details, see see text). O I absorption edge from our Galaxy and various redshifted absorption edges and prominent emission lines from the source are indicated (from Kaastra *et al.* (1989)).

of spectral lines will show the true nature of this soft X-ray excess. Furthermore, there is a hardening of the spectrum below $\sim$ 2 Å, a strong fluorescence line of incompletely iron near 6.4 keV, and sometimes also an Fe absorption edge, all attributed to reprocessing by cool matter (e.g. the accretion disk) surrounding the central hard X-ray source. In some AGN there is evidence for another soft component of presently unknown origin. Optical measurements show that the central region contains dense blobs of cool gas with velocities $\sim$ 100 km/s, the socalled narrow-line region. This soft X-ray component might be optically thin radiation from a hot (10 MK) tenuous intercloud gas pervading most of the central region and in pressure equilibrium with the dense clouds. Figure 17 shows an example of a typical AGN spectrum folded through the response of the high-resolution reflection grating spectrometer on *XMM* (Brinkman *et al.* 1989) as calculated by Kaastra *et al.* (1989). Three components are included: a power law with photon number index -1.7, an optically thin line plus continuum spectrum with T = 10 MK and a modified blackbody component with T = 1 MK. A redshift $z = 0.033$ has been assumed. It is evident that high-resolution X-ray spectroscopy with the capability to detect lines and edges will be the ultimate tool to probe the physical conditions in the central regions of AGN.

7 Various subroutines of the spectral code

Depending on the application to the various possible source configurations we distinguish a number of cases:

1. Multi-temperature plasma (optically thin, steady state, Differential Emission Measure (DEM) modelling)
2. SuperNova Remnant (SNR) (optically thin, multi-temperature structure, transient state)
3. Solar flare plasma (optically thin, transient state)
4. Active-Region-Loop spectrum (ARLS) (optically thin, multi-temperature structure, steady state)
5. (Modified) Black-Body ((M)BB) spectrum (optically thick, single temperature)
6. Power- Law (PL) spectrum (nonthermal)
7. Photo-ionized plasma (nebular type, optically thin/thick)

We will explain the various items.

7.1 DEM modelling technique

To interpret the X-ray and EUV spectra of optically thin sources like stellar coronae and supernova remnants, we use an analyzing technique incorporating the code to model the spectrum from optically thin plasmas in thermal equilibrium and a code to model a temperature structure of the stellar atmosphere or supernova remnant. The method involves three steps:

7.1.1 Optically thin plasma radiation code

During the past decade we have developed a well-known and widely used code based on a theoretical model for spectra emitted by hot, optically thin plasmas. A number of isothermal equilibrium spectra is calculated using the latest version of the Mewe-Gronenschild code for optically thin plasma radiation (e.g. Mewe, Gronenschild, van den Oord 1985a), but extended with spectral lines between 300–2000 Å from Landini and Monsinori Fossi (1990). Usually these spectra are calculated for a logarithmical temperature grid with a range $\log(T[\mathrm{K}]) = 4$–9, and $\Delta \log(T) = 0.05$.

7.1.2 Convolution with the instrument

Each of the spectra produced under §7.1.1 is then transformed into a synthetic *EUVE* observation of an isothermal source with a given emission measure by taking into account the appropiate interstellar absorption, and then convolved with one of the instrument models of the three *EUVE* spectrometers, where the binning and the response and resolution characteristics of these instruments are modelled.

7.1.3 DEM modelling method

7.1.3.1 Iterative Withbroe-Sylwester method

The differential emission measure is defined in §5.3.3. We consistently use here for the DEM in the graphic representations $D(T) \equiv T\varphi(T)\Delta \log(T)$ per interval $\Delta \log(T) = 0.05$ (= grid step of the input spectra generated with the optically thin plasma code).

The DEM is derived from the observed spectrum by deconvolving $T\varphi(T)$ from the measured spectral intensities, using the library of theoretical spectra produced under §7.1.2. For this deconvolution we apply an iterative technique, originally proposed by Withbroe (1975), and significantly modified by Sylwester (Wrocław, Poland) (Sylwester *et al.* 1980), and later on by Fludra (MSSL, UK) (Fludra and Sylwester 1986) to interpret high-resolution X-ray spectra of solar flares. The DEM technique was subsequently extended to broader wavelength ranges by Lemen (Lockheed, Palo Alto), Mewe and Schrijver (Utrecht) and applied to the analysis of our *EXOSAT* transmission grating spectra of various late-type stars (Lemen *et al.* 1989, Schrijver *et al.* 1989).

The method places no restrictions on the functional form of the differential measure distribution, although the final result is subject to an implicit smoothing because spectra with neigbouring values of T are more or less alike. From an analysis of the library of spectra in terms of the mutual correlations it can be shown that the widths in temperature of the correlation functions determine the "temperature resolution", i.e., the scale on which we can extract detail of the DEM distribution. The technique is formulated to exclude *a priori* negative values of the emission measure.

Later on (around 1992) Alkemade and Schrijver developed a software package that originally was intended to be built in SPEX for the analysis of observed *EUVE* spectra and that contains a modified version of the original Sylwester algortihm. The program iterates towards the DEM-function $D_j(T_i)$ which yields a spectrum:

$$f_j^*(\lambda) = \sum_{i=1}^{N} D_j(T_i) F(\lambda, T_i), \tag{6}$$

in which $f_j^*(\lambda)$ is a best fit to the measured spectrum $f(\lambda)$. Here $F(\lambda, T_i)$ is the synthetic spectrum at temperature T_i, and the interval $\Delta \log T = 0.05$. Basically, the algorithm iterates as follows: From a given approximated DEM-function $D_j(T_i)$ the next iteration $D_{j+1}(T_i)$ is found by calculating the following integrals for each spectrum $F(\lambda, T_i)$:

$$I_1(T_i) = \int F(\lambda, T_i) f(\lambda) W(\lambda) d\lambda \quad \text{and} \quad I_2(T_i) = \int F(\lambda, T_i) f_j^*(\lambda) W(\lambda) d\lambda, \tag{7}$$

where $W(\lambda)$ is a carefully constructed weight function, which takes into account the uncertainties in the measured fluxes for every bin of the observed spectrum, considering the counting rate and background. Note that the functions I_1 and I_2 are equivalent to weighted dot products if the involved spectra are interpreted as vectors, so that we are in fact performing a component decomposition. The next iteration of the DEM-modelling then follows from :

$$D_{j+1}(T_i) = D_j(T_i) \ \frac{I_1(T_i)}{I_2(T_i)}. \tag{8}$$

Note: Because the algorithm essentially treats every wavelength bin as a single measurement, and considers the relative weight of each of these measurements, it can easily combine spectra from different wavelength regions in a statistically proper way to find a global best-fit DEM-model.

7.1.3.2 Examples

We have applied a variant of the Withbroe-Sylwester method in a study of DEM models of three prototype cool stars proposed to be observed by the Extreme UltraViolet Explorer (*EUVE*) (e.g. Bowyer *et al.* 1992): (i) Procyon, which has a very cool coronal component with a temperature below 1 MK), model based on *IUE* observations (Jordan *et al.* 1986) and on *EXOSAT*-TGS observations (Lemen *et al.* 1989); (ii) Capella, which possesses a very hot corona with temperatures around 5 and 25 MK, model based on *EXOSAT*-TGS observations (Lemen *et al.* 1989) and *IUE* observations (Doschek and Cowan 1984); (iii) κ^1 Cet as prototype for a Solar-type corona with temperature 2–3 MK, model based on that proposed by Doschek and Cowan (1984) for the quiet Sun, but scaled with *EXOSAT* observations (cf. Mewe 1991a, Table 3) and extended below 1 MK towards lower temperatures using *IUE* data for χ^1 Ori (Jordan *et al.* 1987). For the interstellar density we take: N_H (10^{18} cm^{-2}) = 1.5, 5, and 3 for cases (i), (ii), and (iii), respectively, and for the corresponding absorption cross sections the data from Morrison and McCammon (1983) and Cruddace *et al.* (1974).

With the instrumental data given in the *EUVE* handbook, and using some plausible DEM distributions, we have simulated various test spectra for a standard observing time of 40000 sec., taking into account the estimated sky-background and the statistical Poisson noise. In Figure 18 we have plotted the differential emission measure DEM $\equiv T\varphi(T)\Delta\ln(T)$ per interval $\Delta\ln(T) = 0.115$ (or $\Delta^{10}\log(T) = 0.05$). The results show that by combining the three wavelengths bands (70–200 Å, 100-400 Å and 280–760 Å) we are able to constrain the DEM distribution between ~ 0.05 MK and 10 MK. Outside this temperature region apparently no strong spectral lines are available in the three wavelength bands to constrain the DEM.

7.1.3.3 Inversion method of regularization

In the mean time Schrijver and Alkemade have developed the software using another inversion technique as discussed by Craig and Brown (1986) which uses a second-order regularization (smoothing). This routine has now been built in SPEX and replaces the previously used Sylwester routine (as earlier described in sections 5.3.3, 6.1.3, and 7.1.3). In the document SRON/SPEX/TRPB05 we give a description of the new method (but see also Mewe *et al.* 1994 and Thompson 1991). We stress that the regularization method is not an iterative procedure. An iterative method requires an initial DEM distribution, and, depending on the details of the distribution, the iteration may not converge to the true best–fit solution, but instead may yield a solution corresponding to a local minimum in the χ^2-space (or any other measure of quality that may be used). This problem is avoided by the method of regularization. We have recently applied this technique to the analysis of *EUVE* spectra of a number of cool stars (Mewe *et al.* 1994, Rucinski *et al.* 1994, Schrijver *et al.* 1994).

7.2 Supernova remnants (SNRs)

In the past various subroutines have been developed to describe the hydrodynamical evolution and the non-equilibrium ionization (NEI) in evolving mass elements in a supernova remnant. Descriptions of the basic method in solving the non-equilibrium spatially resolved X-ray spectra of supernova remnants are given by Jansen (1988), Kaastra and Jansen (1992) and Kaastra (1992a). For a short description of the modelling, cf. §6.2.

Once a solution for the hydrodynamic evolution of the SNR has been obtained, the time-dependent ionization balance of the plasma can be determined by solving a set of coupled differential equations describing the population of the ionization states by collisional ionization and radiative and dielectronic recombination (see Eq. (1)). Traditionally such equations are solved by a fourth-order Runge-Kutta

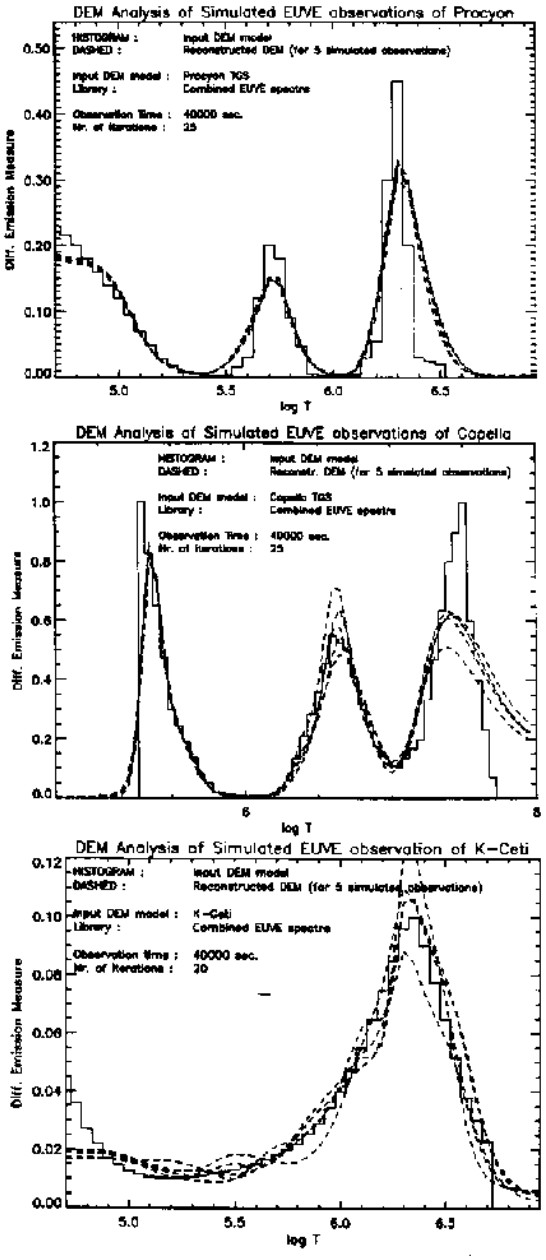

Figure 18: Results of *EUVE* DEM modelling for the models of Procyon (panel a), Capella (b), and κ^1 Cet (c). Plotted vs. temperature T are the values of the differential emission measure DEM $\equiv T\varphi(T)\Delta\ln(T)$ with $\Delta\ln(T) = 0.115$. The input model is shown as a solid histogram and the simulated observations as dashed curves.

scheme, but this requires many evaluations of the transition rates for all (> 200) ions, hence a prohibitive amount of computer time. Kaastra and Jansen have solved this problem by diagonalize the matrix containing the transition rates of ionization and recombination ("eigenvalue decomposition"). This reduces the problem to simple matrix multiplications and exponentiation. Another advantage of this method is that the matrix elements, i.e. the transition rates can be stored on computer disk for a number of temperatures (e.g. for $3 < \log T[\mathrm{K}] < 10$ in steps of $\log T = 0.05$. Such a discretization saves a sizeable amount of computer time.

7.3 Solar and stellar flares

The basic subroutine (NEISPEC) which calculates the non-equilibrium ionization balance and the X-ray spectrum for a given time history of the temperature $T(t)$ and density $n_e(t)$ in a given plasma element must be coupled to a subroutine which calculates a given plasma model (e.g., the hydrodynamical model of the evolution of a SNR) in order to calculate the integrated emergent X-ray spectrum. For the application to cases which may be representative for flares we use either an input file that contains a set of numerical values of T and n_e (or n_H) for a series of time points, or a few standard models that are thought representative of the impulsive and the gradual phase of solar flares: (i) At time $t = 0$ the electron temperature steeply jumps from an initial value T_0 to a constant higher value T_1 ("impulsive burst"); (ii) At $t = 0$ T starts to rise linearly with t from T_0 to a maximum T_1 at $t = t_1$ and thereafter decays exponentially to the initial value ("gradual burst"). Some typical results can be found in publications by Mewe and Schrijver (1978, 1980) and for more detailed calculations for flaring loop models in a paper by Mewe *et al.* (1985b).

7.4 Active-Region-Loop Spectra (ARLS)

Vesecky, Antiochos, and Underwood (1979, hereafter VAU) have developed a computer code to model magnetic loops filled with hot, steady-state plasma. About a decade ago Vesecky has installed the VAU code at MSSL, where it been modified and improved later on by A. Fludra and J.R. Lemen. We use the revised code. An example of the results is given in Figure 12. Schrijver *et al.* (1989) have used the VAU code to fit *EXOSAT*-TGS spectra. In the computations the cross section across the loop can increase with height in a way representing loop-like magnetic field structures by a magnetic line-dipole with the center at a given distance below the chromosphere. In the model this is expressed by an expansion factor $\Gamma > 1$, which is the ratio of the loop cross section at the top to that at the footpoint. In the calculations the base of the loop is placed in the upper chromosphere where $T = 3\ 10^4$ K.

7.5 Blackbody (BB) and Modified Blackbody (MBB) spectra

In the synthetic spectral program which convolves model input spectra with various possible instrument response functions we have built in a module in which various input spectra can be generated. To test for models of active galactic nuclei (AGN) we have created the possibility to calculate combinations of optically thin spectra, power-law (PL) spectra, and blackbody (BB) spectra. As a variant to the BB spectrum we can also calculate a socalled modified BB (MBB) spectrum which is BB radiation modified by repeated inverse Compton scattering by nonrelativistic electrons in a dense medium (e.g. Rybicki and Lightman 1979).

7.6 Power Law (PL) spectra

To describe the X-ray spectrum of the central power source of an AGN we may use the approximation of a PL spectrum. This was built in as an option in the synthetic spectral program.

7.7 Photo-ionized plasmas

This code is currently in development. It is applicable to a gas that is irradiated by a strong X-ray source whose spectrum has to be specified. The ionization structure is set up by a balance between photo-ionization and radiative plus dielectronic recombination, and charge transfer. The energy balance which determines the temperature structure of the illuminated gas is established by a balance between heating and cooling. Heating occurs by photo-ionization, Compton heating, Auger electrons, charge transfer, and collisional de-excitation. Cooling takes place by radiative and dielectronic recombination, continuum bremsstrahlung (inverse Compton cooling), collisional ionization and excitation, and charge transfer.

8 References

Antonucci E., Gabriel, A.H., Acton, L.W., Culhane, J.L., Doyle, J.G., Leibacher, J.W., Machado, M.E., Orwig, L.E., Rapley, C.G.: 1982, *Solar Phys.* **78**, 107

Blumenthal, G.R., Tucker, W.H.: 1974, in: *X-Ray Astronomy,* eds. R. Giacconi, H. Gursky, Reidel Publ. Co., Dordrecht-Holland, p. 99

Bowyer, S., Jelinsky, P., Christian, C.A., Malina, R.F.: 1992, in *The Extreme Ultraviolet Explorer All-Sky Survey and Guest Investigator Spectroscopy Mission*, Proc. Cambridge Workshop on *Stars, Stellar Systems, and the Sun* (Oct. 1991, Tucson, Arizona)

Brinkman, A.C. *et al.*: 1980, *Appl. Optics* **19**, 1601

Brinkman, A.C. *et al.*: 1985, *Adv. Space Res.* **5**, Nr. 3, 65

Brinkman, A.C. *et al.*: 1987, *Astro. Lett. and Communications* **26**, 73

Brinkman, A.C. *et al.*: 1989, in *SPIE EUV, X-Ray, and Gamma-Ray Instrumentation for Astronomy and Atomic Physics,* **1159**, p. 495

Brown, J.C.: 1971, *Solar Phys.* **18**, 489

Cheng, C.-C., Pallavicini, R.: 1991, *Astrophys. J.* **381**, 234

Craig I.J.D., Brown J.C., 1986, *Inverse problems in astronomy,* Bristol: Adam Hilger Ltd, Bristol, England

Cruddace, R., Paresce, F., Bowyer, S., Lampton, M.: 1974, *Astrophys. J.* **187**, 497

Doschek, G.A., Cowan, R.D.: 1984, *Astrophys. J. Suppl. Ser.* **56**, 67

Doschek, G.A., Feldman, U., Cowan, R.D.: 1981, *Astrophys. J.* **245**, 315

Drake, S.A.: 1992, *"Plasma Emission Codes"*, in *Legacy* Nr. 1 (May 1992), the Journal of the High Energy Astrophysics Science Archive Research Center (HEASARC), eds. K.M. Smale, N. White, NASA/GSFC, Greenbelt, U.S.A., p. 59

Elitzur, M.: 1984, *Astrophys. J.* **280**, 653

Elwert, G.: 1952, *Z. Naturf.* **7a**, 432

Feldman, U.: 1981, *Physica Scripta* **24**, 681

Ferland, G.J., Rees, M.J.: 1988, *Astrophys. J.* **332**, 141

Fludra, A., Sylwester, J.: 1986, *Solar Phys.* **105**, 323

Gabriel, A.H.: 1972, *Monthly Not. Roy. Astron. Soc.* **160**, 99

Gabriel, A.H., Jordan, C.: 1969, *Monthly Not. Roy. Astron. Soc.* **145**, 241

Gabriel, A.H., Jordan, C.: 1972, in *Case Studies in Atomic and Collisional Physics* **2**, eds. E.W. McDaniel, M.R.C. McDowell, North-Holland, Amsterdam, p. 209

Gronenschild, E.H.B.M., Mewe, R.: 1978, *Astron. Astrophys. Suppl. Ser.* **32**, 283 (**Paper III**)

Gronenschild, E.H.B.M., Mewe, R.: 1982, *Astron. Astrophys. Suppl. Ser.* **48**, 305
Hamilton, A.J.S., Sarazin, C.L.S., Chevalier, R.A.: 1983, *Astrophys. J. Suppl.* **51**, 115
Heise J.: 1988, in *X-ray Astronomy with EXOSAT,* eds. R. Pallavicini, N.E. White, Memorie della Società Astronomica Italiana **59**, p. 53
Hoover, R.B., Thomas, R.J., Underwood, J.H.: 1972, *Advances in Space Science and Technology* **11**, 1
Itoh, H.: 1984, *Physica Scripta* **T7**, 19
Jakimiec, J., Sylwester, B., Sylwester, J., Serio, S., Peres, G., Reale, F.: 1992, *Astron. Astrophys.* **253**, 269
Jansen, F.A.: 1988, *X-ray photometric morphology of the Cas A and Puppis A supernova remnants* , Thesis, Leiden University
Jordan, C., Ayres, T.R., Brown, A. *et al.*: 1987, *Monthly Not. Roy. Astron. Soc.* **225**, 903
Jordan, C., Brown, A., Walter, F.M., Linsky, J.L.: 1986, *Monthly Not. Roy. Astron. Soc.* **218**, 465
Kaastra, J.S.: 1992a, *An X-ray spectral code for optically thin plasmas* , Internal SRON-Leiden Report, updated version 2.0 12-03-1992
Kaastra, J.S.: 1992b, private communication
Kaastra, J.S., Bleeker, J.A.M.: 1991, in *Iron Line Diagnostics in X-Ray Sources,* eds. A. Treves, G.C. Perola, L. Stella, Lecture notes in Physics **385**, Springer, Berlin, p. 35
Kaastra, J.S., Jansen, F.A.: 1993, *Astron. Astrophys. Suppl. Ser.* **97**, 873
Kaastra, J.S., Mewe, R.: 1993a, *"The Mewe et al. Plasma Emission Code"* , in *Legacy* Nr. 3 (May 1993), the Journal of the High Energy Astrophysics Science Archive Research Center (HEASARC), eds. K.M. Smale, N. White, NASA/GSFC, Greenbelt, U.S.A., p. 16
Kaastra, J.S., Mewe, R.: 1993b, *Astron. Astrophys. Suppl. Ser.* **97**, 443
Kaastra, J.S., Mewe, R.: 1993c, in *UV and X-ray Spectroscopy of Laboratory and Astrophysical Plasmas* , eds. E.H. Silver, S.M. Kahn, Cambridge Univ. Press, Cambridge, U.K., p. 134
Kaastra, J.S., Mewe, R., Brinkman, A.C.: 1989, in Proc. 23d ESLAB Symp. on *Two Topics in X-Ray Astronomy,* ESA SP-296, p. 951
Kahn, S.M., Liedahl, D.A.: 1991, in *Iron Line Diagnostics in X-Ray Sources,* eds. A. Treves, G.C. Perola, L. Stella, Lecture notes in Physics **385**, Springer, Berlin, p. 3
Kallman, T.R., McCray, R.: 1982, *Astrophys. J. Suppl.* **50**, 263
Landini, M., Monsignori Fossi, B.C.: 1990, *Astron. Astrophys. Suppl. Ser.* **82**, 229
Lea, S., Mushotzky, R., Holt, S.S.: 1982, *Astrophys. J.* **262**, 24
Lemen, J.R.: 1992, in Proc. G.S. Vaiana Memorial Symposium on *"Advances in stellar and solar coronal physics"* (June 1992, Palermo), eds. J.R. Linsky, S. Serio, Kluwer Acad. Publ., Dordrecht-Holland, in press
Lemen, J.R., Mewe, R., Schrijver, C.J., Fludra, A.: 1989, *Astrophys. J.* **341**, 474
Liedahl, D.A., Kahn, S.M., Osterheld, A.L., Goldstein, W.H.: 1991, *Astrophys. J.* **350**, L37
Linsky, J.L.: 1985, *Solar Phys.* **100**, 333
Linsky, J.L.: 1990, in *High Resolution X-ray Spectroscopy of Cosmic Plasmas* , eds. P. Gorenstein, M.V. Zombeck, Cambridge Univ. Press, Cambridge, U.K., p. 94
McCray, R.: 1984, *Physica Scripta* **T7**, 73
Mewe, R.: 1970, *Z. Naturf.* **25a**, 1798
Mewe, R.: 1984, *Physica Scripta* **T7**, 5
Mewe, R.: 1988, in *Astrophysical and Laboratory Spectroscopy,* eds. R. Brown, J. Lang, Scottish Univ. Summer School in Phys. Publ., p. 129
Mewe, R.: 1990a, in *Physical Processes in Hot Cosmic Plasmas,* eds. W. Brinkmann, A.C. Fabian, F. Giovanelli, Kluwer Acad. Publ., Dordrecht-Holland, p. 39
Mewe, R.: 1990b, in *Atomic Spectra and Oscillator Strengths for Astrophysics and Fusion,* ed. J.E. Hansen, North-Holland, Amsterdam, p. 67
Mewe, R.: 1991a, *Astron. Astrophys. Rev.* **3**, 127
Mewe, R.: 1991b, *Adv. Space Sci. Rev.* **11**, (1)127
Mewe, R.: 1992, in Proc. Workshop of UK SERC's Collaborative Computational Project No 7 (CCP7), *"Stellar chromospheres, coronae and winds"* (March 1992, Cambridge, U.K.), eds. C.S. Jeffery, R.E.M. Griffin, p. 33
Mewe, R.: 1993, in *"Physics of Solar and Stellar Coronae: G.S. Vaiana Memorial Symposium"* , eds. J.L.

Linsky, S. Serio, Kluwer Acad. Publ., Dordrecht-Holland, p. 225
Mewe, R., Gronenschild, E.H.B.M.: 1981, *Astron. Astrophys. Suppl. Ser.* **45**, 11 (**Paper IV**)
Mewe, R., Gronenschild, E.H.B.M., van den Oord, G.H.J.: 1985a, *Astron. Astrophys. Suppl. Ser.* **62**, 197 (**Paper V**)
Mewe R., Kaastra J.S., Schrijver, C.J., Van den Oord G.H.J., Alkemade, F.J.M., 1994, *Astron. Astrophys.*, in press
Mewe, R., Lemen, J.R., Peres, G., Schrijver, J., Serio, S.: 1985b, *Astron. Astrophys.* **152**, 229
Mewe, R., Lemen, J.R., Schrijver, C.J.: 1991, *Astrophys. Space Sci.* **182**, 35
Mewe, R., Lemen, J.R., van den Oord, G.H.J.: 1986a, *Astron. Astrophys. Suppl. Ser.* **65**, 511 (**Paper VI**)
Mewe, R., Schrijver, C.J., Lemen, J.R., Bentley, R.D.: 1986b, *Adv. Space Res.* **6**, No. 8, 133
Mewe, R., Schrijver, J.: 1978, *Astron. Astrophys.* **65**, 115
Mewe, R., Schrijver, J.: 1980, *Astron. Astrophys.* **87**, 261
Mewe, R., van den Oord, G.H.J., Jakimiec, J.: 1989, in *Solar and Stellar Flares,* eds. B.M. Haisch, M. Rodono, Catania Astrophys. Obs. Special Publ., p. 123
Morrison, R., McCammon, D.: 1983, *Astrophys. J.* **270**, 119
Pallavicini, R., Peres, G., Serio, S., Vaiana, G.S., Golub, L., Rosner, R.: 1981, *Astrophys. J.* **247**, 692
Pasquini, L., Schmitt, J.H.M.M., Pallavicini, R.: 1988, in *Activity in Cool Star Envelopes* , eds. O. Havnes, B.R. Pettersen, J.H.M.M. Schmitt, J.E. Solheim, p. 241
Pradhan, A.K.: 1982, *Astrophys. J.* **263**, 477
Pradhan, A.K.: 1985, *Astrophys. J.* **288**, 824
Pradhan, A.K., Shull, J.M.: 1981, *Astrophys. J.* **249**, 821
Priest, E.R.: 1978, *Solar Phys.* **58**, 57
Raymond, J.C.: 1988, in *Hot Thin Plasmas in Astrophysics,* ed. R. Pallavicini, Kluwer Acad. Publ., Dordrecht-Holland, p. 3
Raymond, J.C.: 1990, in *High Resolution X-ray Spectroscopy of Cosmic Plasmas,* eds. P. Gorenstein, M.V. Zombeck, Proc. IAU Coll. 115, Cambridge, U.S.A., Reidel Publ. Co., Dordrecht-Holland, p. 1
Rosner, R., Tucker, W.M., Vaiana, G.S.: 1978, *Astrophys. J.* **220**, 643 (**RTV**)
Ross, R.R.: 1979, *Astrophys. J.* **233**, 334
Rucinski S.M., Kaastra J.S., Mewe R., Vilhu O., White S.M., 1994, submitted to *Astrophys. J.*
Rybicki, G.B., Lightman, A.P.: 1979, *Radiative Processes in Astrophysics* , John Wiley & Sons, New York
Schmitt, J.H.M.M.: 1990, in *High Resolution X-ray Spectroscopy of Cosmic Plasmas* , eds. P. Gorenstein, M.V. Zombeck, Proc. IAU Coll. 115, Cambridge, U.S.A., Cambridge Univ. Press, Cambridge, p. 110
Schmitt, J.H.M.M., Harnden, F.R., Jr., Peres, G., Rosner, R., Serio, S.: 1985, *Astrophys. J.* **288**, 751
Schrijver, C.J.: 1985, *Space Sci. Rev.* **40**, 3
Schrijver, C.J.: 1987, *Astron. Astrophys.* **180**, 241
Schrijver, C.J., Lemen, J.R., Mewe, R.: 1989, *Astrophys. J.* **341**, 484
Schrijver, C.J., Mewe, R.: 1986, in *Cool Stars, Stellar Systems, and the Sun,* eds. M. Zelik, D.M. Gibson, Springer, New York, p. 300
Schrijver, C.J., Mewe, R., van den Oord, G.H.J. Kaastra, J.S., 1994, in preparation for *Astron. Astrophys.*
Schrijver, C.J., Mewe, R., Walter, F.M.: 1984, *Astron. Astrophys.* **138**, 258
Shapiro, P.R., Moore, R.T.: 1976, *Astrophys. J.* **207**, 460
Shapiro, P.R., Moore, R.T.: 1977, *Astrophys. J.* **217**, 621
Spitzer, L., Jr.: 1962, *Physics of Fully Ionized Gases* (2nd ed.), Intersc. Publ., New York
Švestka, Z.: 1976, *Solar Flares,* Reidel Publ. Co., Dordrecht-Holland
Sylwester, J., Schrijver, J., Mewe, R.: 1980, *Solar Phys.* **67**, 285
Tanaka, K.: 1986, *Publ. Astron. Soc. Japan* **38**, 225
Thompson A.M., 1991, in *Intensity Integral Inversion Techniques: a Study in Preparation for the SOHO Mission* , eds. Harrison R.A., Thompson, A.M., Rutherford Appleton Laboratory Report RAL-91-092, p. 18
Tsuru, T. et al.: 1989, *Publ. Astron. Soc. Japan* **41**, 679
Van den Oord, G.H.J., Mewe, R.: 1989, *Astron. Astrophys.* **213**, 245
Van den Oord, G.H.J., Mewe, R., Brinkman, A.C.: 1988, *Astron. Astrophys.* **205**, 181
Vesecky, J.F., Antiochos, S.K., Underwood, J.H.: 1979, *Astrophys. J.* **233**, 987

Vrtilek, S.D., McClintock, J.E., Seward, F.D., Kahn, S.M., Wargelin, B.J.: 1991, *Astrophys. J. Suppl.* **76**, 1127

White, N.E., Culhane, J.L., Parmar, A.N., Kellett, B.J., Kahn, S., van den Oord, G.H.J., Kuijpers, J.: 1986, *Astrophys. J.* **301**, 262

Wilson, R.: 1962, *J. Quant. Spectr. Rad. Transf.* **2**, 477

Withbroe, G.L.: 1975, *Solar Phys.* **45**, 301

Zhang, J. et al.: 1990, in *High Resolution X-ray Spectroscopy of Cosmic Plasmas* ,eds. P. Gorenstein, M.V. Zombeck, Proc. IAU Coll. 115, Cambridge, U.S.A., Cambridge Univ. Press, Cambridge, p. 361